H0LiCOW – III. Quantifying the effect of mass along the line of sight to the gravitational lens HE 0435−1223 through weighted galaxy counts[★]

Cristian E. Rusu,[1]† Christopher D. Fassnacht,[1]† Dominique Sluse,[2] Stefan Hilbert,[3,4]
Kenneth C. Wong,[5,6] Kuang-Han Huang,[1] Sherry H. Suyu,[6,7,8] Thomas E. Collett,[9]
Philip J. Marshall,[10] Tommaso Treu[11] and Leon V. E. Koopmans[12]

[1]*Department of Physics, University of California, Davis, CA 95616, USA*
[2]*STAR Institute, Quartier Agora - Allée du six Aout, 19c B-4000 Liége, Belgium*
[3]*Exzellenzcluster Universe, Boltzmannstr. 2, D-85748 Garching, Germany*
[4]*Ludwig-Maximilians-Universität, Universitäts-Sternwarte, Scheinerstr. 1, D-81679 München, Germany*
[5]*National Astronomical Observatory of Japan, 2-21-1 Osawa, Mitaka, Tokyo 181-8588, Japan*
[6]*Institute of Astronomy and Astrophysics, Academia Sinica (ASIAA), PO Box 23-141, Taipei 10617, Taiwan*
[7]*Max-Planck-Institut für Astrophysik, Karl-Schwarzschild-Str. 1, D-85748 Garching, Germany*
[8]*Physik-Department, Technische Universität München, James-Franck-Straße 1, D-85748 Garching, Germany*
[9]*Institute of Cosmology and Gravitation, University of Portsmouth, Burnaby Rd, Portsmouth PO1 3FX, UK*
[10]*Kavli Institute for Particle Astrophysics and Cosmology, Stanford University, 452 Lomita Mall, Stanford, CA 94035, USA*
[11]*Department of Physics and Astronomy, University of California, Los Angeles, CA 90095-1547, USA*
[12]*Kapteyn Astronomical Institute, University of Groningen, PO Box 800, NL-9700 AV Groningen, The Netherlands*

ABSTRACT

Based on spectroscopy and multiband wide-field observations of the gravitationally lensed quasar HE 0435−1223, we determine the probability distribution function of the external convergence κ_{ext} for this system. We measure the under/overdensity of the line of sight towards the lens system and compare it to the average line of sight throughout the Universe, determined by using the CFHTLenS (The Canada France Hawaii Lensing Survey) as a control field. Aiming to constrain κ_{ext} as tightly as possible, we determine under/overdensities using various combinations of relevant informative weighting schemes for the galaxy counts, such as projected distance to the lens, redshift and stellar mass. We then convert the measured under/overdensities into a κ_{ext} distribution, using ray-tracing through the Millennium Simulation. We explore several limiting magnitudes and apertures, and account for systematic and statistical uncertainties relevant to the quality of the observational data, which we further test through simulations. Our most robust estimate of κ_{ext} has a median value $\kappa_{\mathrm{ext}}^{\mathrm{med}} = 0.004$ and a standard deviation $\sigma_\kappa = 0.025$. The measured σ_κ corresponds to 2.5 per cent relative uncertainty on the time delay distance, and hence the Hubble constant H_0 inferred from this system. The median $\kappa_{\mathrm{ext}}^{\mathrm{med}}$ value varies by ~ 0.005 with the adopted aperture radius, limiting magnitude and weighting scheme, as long as the latter incorporates galaxy number counts, the projected distance to the main lens and a prior on the external shear obtained from mass modelling. This corresponds to just ~ 0.5 per cent systematic impact on H_0. The availability of a well-constrained κ_{ext} makes HE 0435−1223 a valuable system for measuring cosmological parameters using strong gravitational lens time delays.

Key words: gravitational lensing: strong – methods: statistical – quasars: individual: HE 0435−1223 – cosmological parameters – distance scale.

1 INTRODUCTION

When a source with time-varying luminosity is multiply-imaged by strong gravitational lensing, the time delays between its images can be used to measure cosmological distances and the Hubble

constant H_0 (Refsdal 1964). In particular, for a lens system with a strong deflector at a single redshift, one may infer the 'time-delay distance'

$$D_{\Delta t} = (1 + z_d) \frac{D_d D_s}{D_{ds}}, \tag{1}$$

where z_d denotes the redshift of the foreground deflector, D_d the angular diameter distance to the deflector, D_s the angular diameter distance to the source and D_d^s the angular diameter distance between the deflector and the source. The time-delay distance is primarily sensitive to the Hubble constant, i.e. $D_{\Delta t} \propto H_0^{-1}$ (see Treu & Marshall 2016, for a recent review).

Inferring cosmological distances from measured time delays also requires accurate models for the mass distribution of the main deflector and its environment, as well as for any other matter structures along the line of sight that may influence the observed images and time delays (Suyu et al. 2010). Galaxies very close in projection to the main deflector often cause measurable higher-order perturbations in the lensed images and time delays and require explicit models of their matter distribution. The effect of galaxies more distant in projection is primarily a small additional uniform focusing of the light from the source. Furthermore, matter underdensities along the line of sight such as voids, indicated by a low galaxy number density, cause a slight defocusing. For a strong lensing system with a main deflector at a single redshift, the net effect of the (de)focusing by these weak perturbers is equivalent (to lowest relevant order) to that of a constant external convergence[1] term κ_{ext} in the lens model for the main deflector (Suyu et al. 2010). This implies on the one hand that the weak perturbers' effects, i.e. the external convergence they induce, cannot be inferred from the observed strongly lensed image properties alone due to the 'mass-sheet degeneracy' (MSD; Falco, Gorenstein & Shapiro 1985; Schneider & Sluse 2013). On the other hand, if the external convergence is somehow determined from ancillary data, and a time-delay distance $D_{\Delta t}^{(0)}$ has been inferred using a model not accounting for the effects of weak perturbers along the line of sight, the true time-delay distance $D_{\Delta t}$ can simply be computed by:

$$D_{\Delta t} = \frac{D_{\Delta t}^{(0)}}{1 - \kappa_{ext}}. \tag{2}$$

This relation makes clear that any statistical and systematic uncertainties in the external convergence due to structures along the line of sight directly translate into statistical and systematic errors in the inferred time delay distance and Hubble constant:

$$H_0 = (1 - \kappa_{ext}) H_0^{(0)}, \tag{3}$$

where $H_0^{(0)}$ denotes the Hubble constant inferred when neglecting weak external perturbers. With reduced uncertainties on other component of the time delay distance measurement from state-of-the-art imaging, time-delay measurements, and modelling techniques of strong lens systems, the external convergence κ_{ext} is now left as an important source of uncertainty on the inferred H_0, contributing up to ∼5 per cent to the error budget on H_0 (Suyu et al. 2010, 2013). Moreover, the mean external convergence may not vanish for an ensemble of lens systems due to selection effects, causing a slight preference for lens systems with overdense lines of sights (Collett & Cunnington 2016). Thus, an ensemble analysis simply assuming $\kappa_{ext} = 0$ is expected to systematically overestimate the Hubble constant H_0.

Accurately quantifying the distribution of mass along the line of sight requires wide-field imaging and spectroscopy (e.g. Keeton & Zabludoff 2004; Fassnacht et al. 2006; Momcheva et al. 2006; Fassnacht, Koopmans & Wong 2011; Wong et al. 2011, see Treu & Marshall 2016 for a recent review). Suyu et al. (2010) pioneered the idea of estimating a probability distribution function $P(\kappa_{ext})$ by (i) measuring the galaxy number counts around a lens system, (ii) comparing the resulting counts against those of a control field to obtain relative counts and (iii) selecting lines of sight of similar relative counts, along with their associated convergence values, from a numerical simulation of cosmic structure evolution. To this end, Fassnacht et al. (2011) measured the galaxy number counts in a 45 arcsec aperture around HE 0435−1223 [α(2000): 04^{h}38^{m}14^{s}9, δ(2000): −12°17′14″.4; Wisotzki et al. 2000, 2002; lens redshift $z_d = 0.455$; Morgan et al. (2005); source redshift $z_s = 1.693$; Sluse et al. (2012)], and found that it is 0.89 of that on an average line of sight through their ∼0.06 deg^2 control field. Both Greene et al. (2013, hereafter G13) and Collett et al. (2013) find that $P(\kappa_{ext})$ can be most precisely constrained for lens systems along underdense lines of sight, making HE 0435−1223 a valuable system.

Recent work has focused on tightening the constraints on $P(\kappa_{ext})$ with data beyond simple galaxy counts. Suyu et al. (2013) used the external shear inferred from lens modelling as a further constraint, which significantly affected the inferred external convergence due to the large external shear required by the lens model. G13 extended the number counts technique by considering more informative, physically relevant weights, such as galaxy redshift, stellar mass and projected separation from the line of sight. Both of these works used ray-tracing through the Millennium Simulation (MS; Springel et al. 2005; Hilbert et al. 2009) in order to obtain $P(\kappa_{ext})$. For lines of sight which are either underdense or of common density, G13 found that the residual uncertainty $\sigma_{\kappa_{ext}}$ on the external convergence can be reduced to ≲0.03, which corresponds to an uncertainty on time delay distance and hence H_0 comparable to that arising from the mass model of the deflector and its immediate environment. Furthermore, Collett et al. (2013) considered a reconstruction of the mass distribution along the line of sight using a galaxy halo model. They convert the observed environment around a lens directly into an external convergence, after calibrating for the effect of dark structures and voids by using the MS.

We have collected sufficient observational data to implement these techniques for the case of HE 0435−1223. We choose to adopt the G13 approach, with several improvements. We first aim to understand and account for various sources of error in our observational data for HE 0435−1223, as well as that of CFHTLenS (The Canada France Hawaii Lensing Survey; Heymans et al. 2012), which we choose as our control field. Secondly, we incorporate our understanding of these uncertainties into the simulated catalogues of the MS, in order to ensure a realistic estimate of $P(\kappa_{ext})$. Thirdly, we use the MS to test the robustness of this estimate for simulated fields of similar under/overdensity.

This paper is organized as follows. In Section 2 we present the relevant observational data for HE 0435−1223 and its reduction. In Section 3 we present an overview of our control field, CFHTLenS. In Section 4 we present our source detection, classification, photometric redshift and stellar mass estimation, carefully designed to match the CFHTLenS fields. In Section 5 we present our technique to measure weighted galaxy count ratios for HE 0435−1223, by accounting for relevant errors. In Section 6 we use ray-tracing through the MS in order to obtain $P(\kappa_{ext})$ for the measured ratios, and present our tests for robustness. We present and discuss our results in

---

[1] The external convergence κ_{ext} may be positive or negative depending on whether focusing or defocusing outweighs the other.

Table 1. Summary of observations.

Telescope/instrument	FOV [arcmin]/scale [arcsec]	Filter	Exposure (s)	Airmass	Seeing (arcsec)	Observation date
CFHT/MegaCam	$58 \times 56/0.187$	u	41×440	1.2–1.5	~ 0.8	2014 Aug. 31–Sept. 2
Subaru/Suprime-Cam	$34 \times 27/0.200$	g	5×120	1.7–1.8	~ 0.7	2014 Mar. 1
Subaru/Suprime-Cam	$34 \times 27/0.200$	r	16×300	1.2–1.6	~ 0.7	2014 Mar. 1
Subaru/Suprime-Cam	$34 \times 27/0.200$	i	5×120	2.0–2.2	~ 0.8	2014 Mar. 1
Gemini North/NIRI	$3.4 \times 3.4/0.116$	J	44×42.2	1.2–1.3	~ 0.4	2012 Aug. 22
Subaru/MOIRCS	$4 \times 7/0.116$	H	12×78	1.7–2.1	~ 0.7	2015 Apr. 1
Gemini North/NIRI	$3.4 \times 3.4/0.116$	K_s	32×32.2	1.2–1.3	~ 0.4	2012 Aug. 22
Spitzer/IRAC	$5.2 \times 5.2/0.6$	3.6	72×30	–	–	2006 Feb. 8, 2006 Sept. 20
Spitzer/IRAC	$5.2 \times 5.2/0.6$	4.5	72×30	–	–	2006 Feb. 8, 2006 Sept. 20
Spitzer/IRAC	$5.2 \times 5.2/0.6$	5.8	72×30	–	–	2006 Feb. 8, 2006 Sept. 20
Spitzer/IRAC	$5.2 \times 5.2/0.6$	8.0	72×30	–	–	2006 Feb. 8, 2006 Sept. 20

Note. For NIRI, where the instrument FOV is just 2×2 arcmin^2, 'FOV' refers to the effective field of view on the sky, after dithering. For IRAC, the filters denote the effective wavelengths in μm.

Section 7, and we conclude in Section 8. We present additional details in the Appendix.

The current work represents Paper III (hereafter H0LiCOW Paper III) in a series of five papers from the H0LiCOW collaboration, which together aim to obtain an accurate and precise estimate of H_0 from a comprehensive modelling of HE 0435−1223. An overview of this collaboration can be found in H0LiCOW Paper I (Suyu et al. 2017), and the derivation of H_0 is presented in H0LiCOW Paper V (Bonvin et al. 2017).

Throughout this paper, we assume the MS cosmology, $\Omega_m = 0.25$, $\Omega_\Lambda = 0.75$, $h = 0.73$, $\sigma_8 = 0.9$.[2] We present all magnitudes in the AB system, where we use the following conversion factor between the Vega and the AB systems: $J_{AB} = J_{Vega} + 0.91$, $H_{AB} = H_{Vega} + 1.35$ and $K_{s\,AB} = K_{s\,Vega} + 1.83$.[3] We define all standard deviations as the semi-difference between the 84 and 16 percentiles.

2 DATA REDUCTION AND CALIBRATION

In order to characterize the HE 0435−1223 field, we require a catalogue of galaxy properties, such as galaxy redshifts and stellar masses. To this end, we have obtained multiband, wide-field imaging observations of HE 0435−1223, from ultraviolet to near/mid-infrared wavelengths. The observations are detailed in Table 1, and were obtained with the Canada–France–Hawaii Telescope (CFHT; PI. S. Suyu), the Subaru Telescope (PI. C. Fassnacht) and the Gemini North Telescope (PI. C. Fassnacht). We also use archival *Spitzer* Telescope data (PI. C. Kochanek, Program ID 20451). In addition, we make use of a number of secure spectroscopic redshifts (374 and 43 objects inside an $\sim$17- and 2-arcmin-radius circular aperture, respectively, not counting the lens itself), obtained with the Magellan 6.5-m telescope (Momcheva et al. 2006, 2015), the VLT (PI: Sluse), the Keck Telescope (PI: Fassnacht), and the Gemini Telescope [PI: Treu; see H0LiCOW Paper II (Sluse et al. 2017) for details on the spectroscopic observations]. Those data provide a spectroscopic identification of $\sim$90 per cent ($\sim$60 per cent) of the galaxies down to $i = 21$ mag ($i = 22$ mag) within a radius of 2 arcmin of the lens, namely the maximum radius within which we calculate weighted number counts in this work (see fig. 3 of H0LiCOW Paper II for spectroscopic completeness as a function of radius/magnitude).

We reduced the imaging data using standard reduction techniques. We obtained the CFHT MegaCam (Boulade et al. 2003) and *Spitzer* Infrared Array Camera (IRAC; Fazio et al. 2004) data already pre-reduced and photometrically calibrated. We used SCAMP (Bertin 2006) to achieve consistent astrometric and photometric calibration, and SWARP (Bertin et al. 2002) to resample the data on a 0.2 arcsec pixel scale, using a tangential projection. This is the native pixel scale of Subaru Suprime-Cam (Miyazaki et al. 2002), and the largest among the available data, with the exception of IRAC (0.600 arcsec pixel scale).

We reduced the Subaru MOIRCS (Ichikawa et al. 2006; Suzuki et al. 2008) data using a pipeline provided by Ichi Tanaka, based on IRAF.[4] For the Gemini NIRI (Hodapp et al. 2003) and Subaru MOIRCS data we calibrated the photometry using 2MASS stars in the field of view (FOV). For Subaru Suprime-Cam, we used observations of a Sloan Digital Sky Survey (SDSS) star field, taken the same night. We excluded stars with nearby companions that can affect the SDSS photometry, and used colour transformations provided by Yagi Masafumi [private communication; also described in Yagi et al. (2013a,b)], in order to calibrate the photometry to the AB system. We corrected for galactic and atmospheric extinction following Schlafly & Finkbeiner (2011) and Buton et al. (2012), respectively. We present our strategy for source detection, classification, redshift and stellar mass estimation in Section 4.

3 THE CONTROL FIELD: CFHTLENS

In order to apply the weighted number counts technique, we need a control field against which to determine an under/overdensity. We require the field to be of a suitable depth, as well as larger in spatial extent than the $\sim$0.06 deg^2 field used by Fassnacht et al. (2011), or the 1.21 deg^2 Cosmic Evolution Survey (COSMOS; Scoville et al. 2007), which is known to be overdense (e.g. Fassnacht et al. 2011, and references within). The field should consist of several fields spread across the sky, in order to account for sample variance, and should also contain high to medium resolution, well-calibrated multiband data for object classification, and to infer photometric redshifts and stellar masses reliably.

---

[2] We estimate the impact of using a different cosmology in Appendix D.
[3] Results based on the MOIRCS filters, available at http://www.astro.yale.edu/eazy/filters/v8/FILTER.RES.v8.R300.info.txt

[4] IRAF is distributed by the National Optical Astronomy Observatory, which is operated by the Association of Universities for Research in Astronomy (AURA) under cooperative agreement with the National Science Foundation.

Such a field is provided by the wide component of the CFHT Legacy Survey (CFHTLS; Gwyn 2012). It consists of *ugriz* imaging over four distinct contiguous fields: W1 ($\sim$63.8 deg^2), W2 ($\sim$22.6 deg^2), W3 ($\sim$44.2 deg^2) and W4 ($\sim$23.3 deg^2), with typical seeing $\sim$0.7 arcsec in *i* band. The data have been further processed, and are available in catalogue form from CFHTLenS (Heymans et al. 2012). We provide here a summary of the CFHTLenS data quality and products that are relevant to our analysis. CFHTLenS reaches down to 24.54 ± 0.19 5σ limiting magnitude in a 2.0 arcsec aperture in the deepest band, *i* (Erben et al. 2013). The photometry has been homogenized through matched and Gaussianized point-spread functions (PSFs) (Hildebrandt et al. 2012), leading to well-characterized photometric redshifts. The CFHTLenS catalogue includes best-fitting photometric redshifts derived with BPZ (Benítez 2000), and best-fitting stellar masses computed with LE PHARE (Ilbert et al. 2006). The final product has a spectroscopic to photometric redshift scatter $\sigma_{|z_{\rm spec}-z_{\rm phot}|/(1+z_{\rm spec})}$ of $\lesssim$0.04 for *i* < 23 ($\lesssim$0.06 for *i* < 24). The outlier fraction[5] is $\lesssim$5 per cent for *i* < 23 ($\lesssim$15 per cent for *i* < 24) (Hildebrandt et al. 2012).

The object detection and measurement are summarized by Erben et al. (2013): SEXTRACTOR (Bertin & Arnouts 1996) is run six times in dual-image mode. In five of the runs, the detection image is the deeper image band (*i*), and the measurement images are the PSF-matched images in each of the five bands; in the sixth run, the measurement image is the original lensing band image. This last run is performed to obtain total magnitudes (SEXTRACTOR quantity MAG_AUTO) in the deepest band, whereas the first five runs yield accurate colours based on isophotal magnitudes (MAG_ISO).

The galaxy–star classification is summarized by Hildebrandt et al. (2012), who also estimate its uncertainty, quantified in terms of incompleteness and contamination, based on a comparison with spectroscopic data from the VVDS F02 (Le Fèvre et al. 2005, reaching down to *i* = 24 mag) and VVDS F22 (Garilli et al. 2008) surveys. In brief, for *i* < 21, objects with size smaller than the PSF are classified as stars. For *i* > 23, all objects are classified as galaxies. In the range 21 < *i* < 23, an object is defined as a star if its size is smaller than the PSF, and in addition $\chi^2_{\rm star} < 2.0\chi^2_{\rm gal}$, where χ^2 is the best-fitting goodness-of-fit χ^2 from the galaxy and star libraries given by LE PHARE.

4 MEASURING PHYSICAL PROPERTIES OF GALAXIES

4.1 Detecting and measuring sources with SEXTRACTOR

In order to avoid introducing biases in measuring weighted number counts, it is important to adopt detection, measuring and classification techniques for the HE 0435–1223 field that are as close as possible to those of CFHTLenS, while also assessing the similarities between the two data sets.

The HE 0435–1223 *ugri* data are similar in terms of seeing to those from CFHTLenS (Table 1). The pixel scales of the two data sets differ by only 6.5 per cent. In terms of depth, the limiting magnitude of the HE 0435–1223 data in *i* band, following the definition in Erben et al. (2013),[6] is 24.55 ± 0.17, thus virtually indistinguish-

able from the counterpart band in CFHTLenS (Section 3). The limiting magnitudes in the other bands are, respectively, 25.55 ± 0.06 (*u*), 25.43 ± 0.20 (*g*), 25.94 ± 0.28 (*r*), 22.71 ± 0.13 (*J*), 21.20 ± 0.28 (*H*), 21.82 ± 0.28 (K_s), and can be compared with the available counterparts in table 1 of Erben et al. (2013). In particular, our deepest image (*r* band) is $\sim$1 mag deeper than the CFHTLenS *r* band.

To infer accurate photometry, we matched the PSFs in the *griJHK$_s$* images to that in the *u* band, which has the largest seeing. We combined bright, unsaturated stars across the FOV in each band, in order to build their PSFs. We replaced the noisy wings with analytical profiles, and computed convolution kernels using the Richardson–Lucy deconvolution algorithm (Richardson 1972; Lucy 1974).

Our primary region of interest is a 4×4 arcmin^2 area around HE 0435–1223, as for this area we have (for the most part) uniform coverage in all bands, including IRAC. However, it is important to also consider a larger area, in order to use as many spectroscopically observed galaxies as possible for calibrating photometric redshifts. In addition, a wider area is necessary for identifying groups/clusters (H0LiCOW Paper II), and performing a weak lensing analysis (Tihhonova et al., in preparation). As a result, we are also interested in the whole coverage of the *ugri* frames.

Before using SEXTRACTOR in a similar way to CFHTLenS on the 4×4 arcmin^2 images, we masked bright stars that are heavily saturated in *r* band. We found that by fitting and subtracting a Moffat profile to these bright stars, we can reduce the contamination of nearby objects by the bright stars, and improve the detection parameters; this minimizes the area that needs to be masked in the *r* band, but which is unaffected in most of the other bands. We convolve the masks with a narrow Gaussian, in order to smooth their edges, which would otherwise produce spurious detections. We also set a mask of 5 arcsec radius around the HE 0435–1223 system itself, in order to account for the fact that the external convergence of the most nearby galaxy is accounted for explicitly in the lens mass modelling in H0LiCOW Paper IV.

Despite our *r* band being deeper, given the fact that CFHTLenS performed detections in *i*, and the similarity of our *i*-band frame to the CFHTLenS *i* band, we first performed detections in the unconvolved (pre-PSF matching) *i* image. For this, we ran SEXTRACTOR with the same detection parameters used by CFHTLenS (Jean Coupon, private communication). The purpose of this run is to estimate total magnitudes MAG_AUTO in this band, which we use when performing magnitude cuts at our faint threshold. However, for the purpose of extracting reliable photometry to be used for photometric redshift and stellar mass estimation, since measurements are expected to be more reliable in *r* band (with an exception being around bright objects, which appear brighter than in *i*), we also perform detections in this band, using optimized SEXTRACTOR detection parameters. As for measurements, we perform them as described for CFHTLenS in Section 3. We infer final MAG_ISO magnitudes, corrected for total magnitude, following CFHTLenS, as MAG_ISO$_x$ + (MAG_AUTO$_r$ − MAG_ISO$_r$), where the subscript refers to the measurement band ($x = u, g, r, i, J, H, K_s$). We make an exception for $\sim$17 per cent of objects, which have a SEXTRACTOR flag indicative of unreliable MAG_AUTO, and for which we replace MAG_AUTO with MAG_ISO. For the FOV outside 4×4 arcmin^2, which is used for separate purposes by H0LiCOW Paper II and Tihhonova et al. (in preparation) we performed all detections in the *r* band only. We find that galaxies with $i \lesssim 24$ mag are typically detected in all bands, with the exception of 18 per cent in *JK$_s$*, where the spatial coverage is also reduced, and $\sim$6 per cent in *u* band.

---

[5] The outliers are defined as galaxies with $|z_{\rm spec}-z_{\rm phot}|/(1+z_{\rm spec}) < 15$.

[6] $m_{\rm lim} = {\rm ZP} - 2.5 \log \left(5\sqrt{N_{\rm pix}}\sigma_{\rm sky} \right)$, where ZP is the magnitude zeropoint, $N_{\rm pix}$ is the number of pixels in a circle with radius 2.0 arcsec, and $\sigma_{\rm sky}$ is the sky-background noise variation. We derive the uncertainty as the standard deviation of the values in 10 empty regions across the frame.
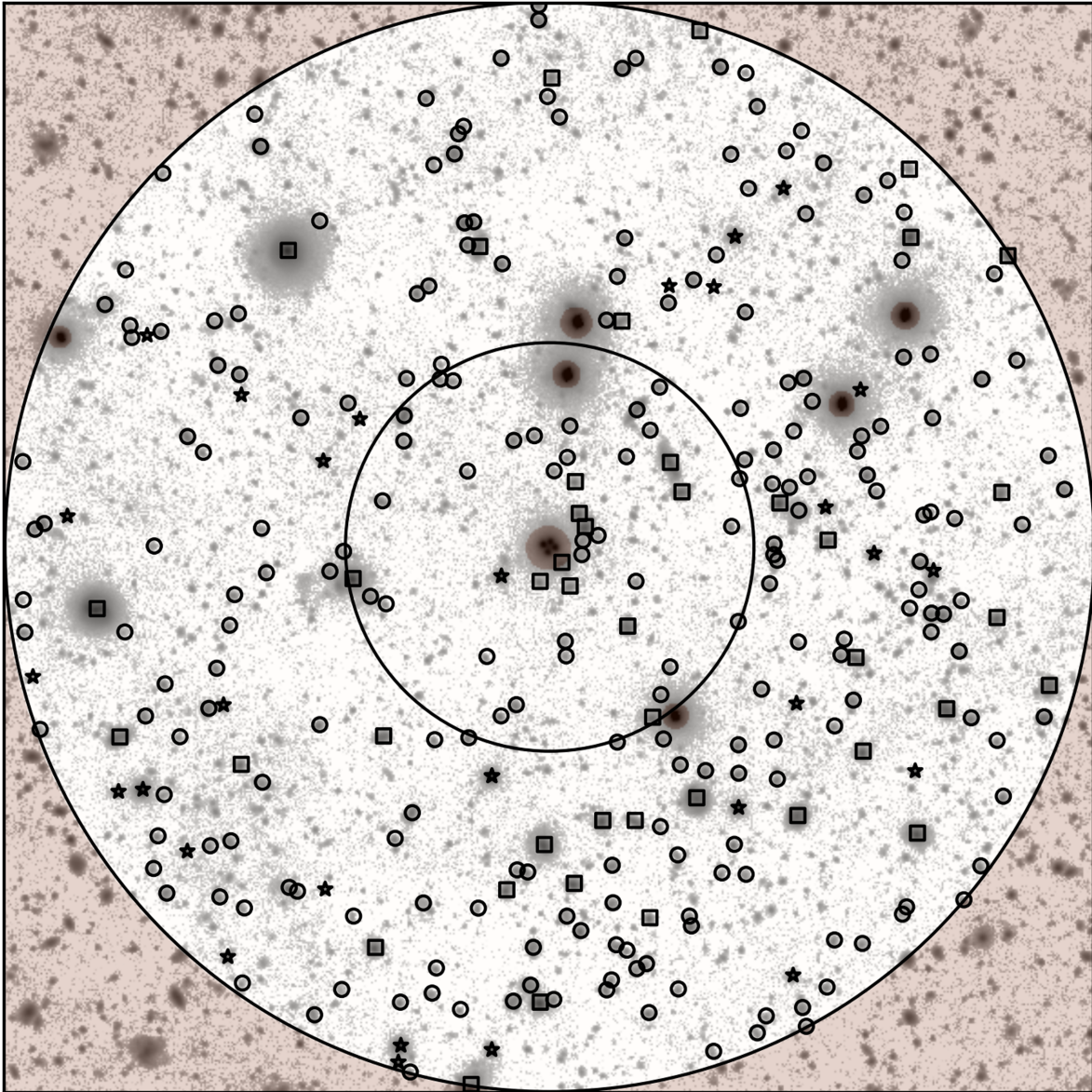
Figure 1. 4×4 arcmin^2 FOV for HE 0435−1223 in the deepest band, *r*. North is up and East is to the left. The $i < 24$ objects identified by SEXTRACTOR inside a 120 arcsec aperture are marked: star symbols for stars, circles for galaxies without spectroscopic redshift and squares for galaxies with spectroscopic redshift. HE 0435−1223 is at the centre of the field. Brown regions represent masks outside the aperture, around the lensed system and around bright, saturated stars. The two concentric black circles mark the 45 and 120 arcsec apertures, respectively. The nearest galaxy to the centre, towards SE, is located inside the mask, as it is modelled explicitly in H0LiCOW Paper IV (Wong et al. 2017). For an extended FOV in *i* band, see H0LiCOW Paper II.

We use T-PHOT (Merlin et al. 2015) to extract MAG_ISO magnitudes, and thus measure colours between optical and IRAC filters, as the latter have vastly different pixel scale and PSFs. For this, we use the *r*-band image as position and morphology prior. Finally, we apply the same star–galaxy classification used by CFHTLenS.

Table A1 compiles the $i < 23$ galaxies detected in a 45-arcsec-radius aperture around HE 0435−1223, along with their measured photometry. The $i < 24$ galaxies in a 120-arcsec-radius aperture can be found in the accompanying online material, and are marked in Fig. 1.

4.2 Galaxy–star separation, redshifts and stellar masses

Using the PSF-matched photometry measured with SEXTRACTOR, we infer photometric redshifts and stellar masses, which we will later use as weights. We further calibrate our magnitudes by finding the zero-points which minimize the scatter between photometric and spectroscopic redshifts of the $17 < i < 23$ mag galaxies with available spectroscopy. Finally, we perform a robust galaxy–star classification using morphological as well as photometric information. For measuring redshifts, we primarily use BPZ, which was also employed by CFHTLenS. However, we also use EAZY (Brammer, van Dokkum & Coppi 2008), to assess the dependence on a particular code/set of templates.

For the purpose of estimating photometric redshifts we ignore the IRAC channels, as e.g. Hildebrandt et al. (2010) note that the use of currently available mid-IR templates degrades rather than improves the quality of the inferred redshifts. For both BPZ and EAZY, we obtained the best results when using the default set of templates (CWW+SB and a linear combination of principal component
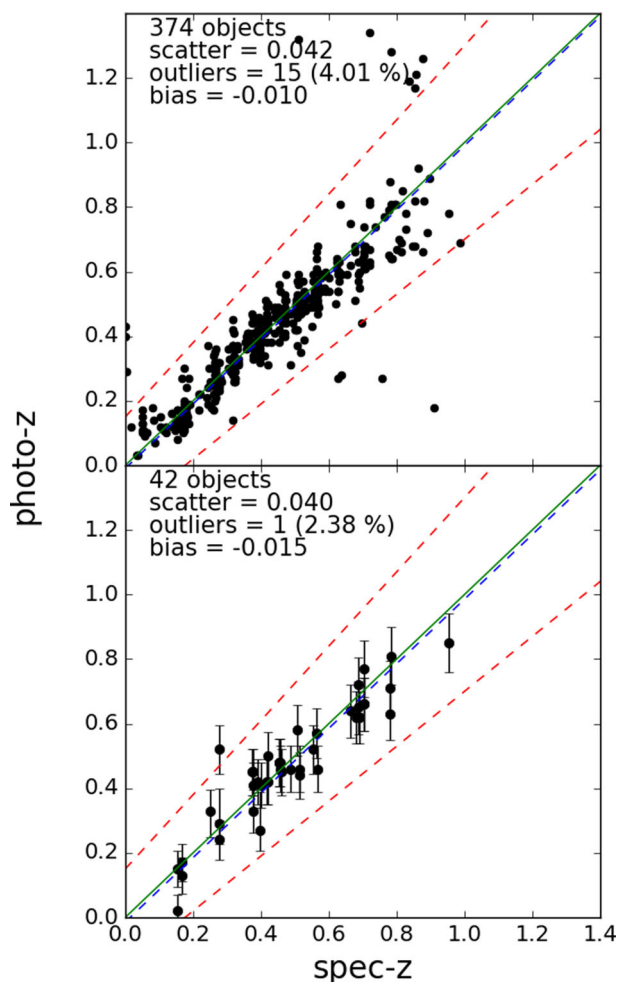
Figure 2. Comparison of spectroscopic and photometric (BPZ) redshifts for all galaxies with robust spectroscopic redshifts within the Suprime-Cam FOV (top, *ugri*), as well as for the galaxies within 120 arcsec (bottom, *ugriJHK*). The blue dashed line represents the best-fitting offset. We define the outliers, located outside the red dashed line, as $|z_{spec} - z_{phot}|/(1 + z_{spec}) > 0.15$, and mark this with red dashed lines. On the bottom plot, error bars refer to 1σ uncertainties determined with BPZ.

spectra, respectively), with the default priors. Fig. 2 compares the available spectroscopic redshifts with the inferred photometric redshift for the *ugriJHK$_s$* and *ugri* filters, and galaxies with $i < 24$ mag. There is negligible bias, and the scatter/outlier fractions are comparable to or smaller than the ones for CFHTLenS (Section 3). In addition, Fig. B1 compares the BPZ- and EAZY-estimated redshifts, for the $i < 24$ galaxies inside the 4×4 arcmin^2 region around HE 0435−1223, showing a good overall match. We also tested whether our choice of different templates and prior, compared to those used to determine photometric redshifts for CFHTLenS, can potentially introduce systematics. For this, we recalculated photometric redshifts for ∼400 000 galaxies in CFHTLenS, down to $i < 24$ mag. After imposing the condition $z < z_s$, where z_s is the HE 0435−1223 source quasar redshift, this resulted in a negligible 0.03 offset compared to the CFHTLenS-derived values, with scatter and outlier fractions similar to those found by Hildebrandt et al. (2012) (see Section 3).

For estimating stellar masses, we followed the approach by Erben et al. (2013), which was also used to produce the CFHTLenS catalogues. This uses templates based on the stellar population syn-

thesis package of Bruzual & Charlot (2003), with a Chabrier (2003) initial mass function [see Velander et al. (2014) for additional details], and fits stellar masses with LE PHARE, at fixed redshift. We performed the computation twice, without and with using the IRAC photometry. In the latter case, we boosted the photometric errors to account for the template error derived by Brammer et al. (2008). We find only small scatter (∼0.05 in log $M_\star$) and no bias, in agreement with the results of Ilbert et al. (2010) for a similar redshift range. The resulting redshifts and the stellar masses are given in Table A2. We used the median of the mass probability distribution as our estimate, except for a few per cent of galaxies where LE PHARE fails to give a physical estimate for this, and we use the best-fitting value instead. This is also the case for the CFHTLenS catalogues, where we recomputed stellar masses in order to fix the ∼6 per cent of objects with missing estimates. In fact, we recomputed stellar masses for the whole CFHTLenS catalogues, in order to use the same cosmology employed by the MS.

Finally, following the recipe from Section 3, we performed a galaxy–star classification. As described in more detail by Hildebrandt et al. (2012), we estimated the PSF size as the 3σ upper cut half light radius estimated by SEXTRACTOR in *r* band, and we used all available bands when computing the goodness-of-fit. Comparing to the available spectroscopic data, we find that all spectroscopically confirmed galaxies are correctly classified as galaxies, whereas three spectroscopically confirmed stars, with blended galaxy contaminants, are incorrectly classified as galaxies. We therefore removed them.

## 5 DETERMINING LINE-OF-SIGHT UNDER/ OVERDENSITIES USING WEIGHTED NUMBER COUNTS

5.1 Description of the technique

Fassnacht et al. (2011) computed lens field overdensities as galaxy count ratios by first measuring the mean number counts in a given aperture through their control field, and then dividing the counts in the same aperture around the lens to the mean, i.e. $\zeta_{gal} \equiv N_{gal}/\overline{N_{gal}}$. The situation is more complicated for us because (1) we are interested in using weights dependent on the particular galaxy position inside the aperture, and (2) the CFHTLenS control fields contain a large fraction of masks throughout. These masked areas are due to luminous haloes around saturated stars, asteroid trails, flagged pixels, etc. (Erben et al. 2013).

Therefore, to implement our galaxy weighting schemes, we first divide each of the W1–W4 CFHTLenS fields into a two-dimensional, contiguous grid of cells, of the same size as the apertures we consider around HE 0435−1223. We apply the CFHTLenS masks, at their particular position inside the cell, to the HE 0435−1223 field as well. Thus, when measuring weighted counts, we test whether each galaxy in the HE 0435−1223 field is located at a position which is covered by a mask in a particular cell. Conversely, we also test whether a galaxy in the cell is covered by a mask in the HE 0435−1223 field. This technique is depicted in Fig. 3.

We divide the weighted counts measured around HE 0435−1223 to those measured in the same way around the centre of each of the cells in the CFHTLenS grid, and consider the median of these divisions as our estimate of the overdensity. We justify the use of the median in Section 5.2 and Appendix C. Formally, ζ_{gal} then becomes $\overline{\zeta_{gal}^{WX}} \equiv \mathrm{median}(N_{gal}^{lens,mask_i}/N_{gal}^{WX,i})$, where $X = 1, ..., 4$ and i spans
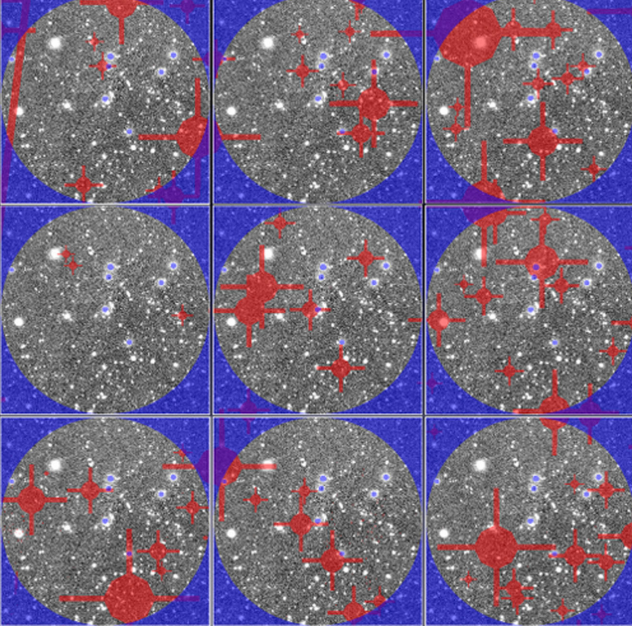
Figure 3. Schematic of the way masking is applied when matching the HE 0435−1223 and various CFHTLenS subfields, on a grid. The 2-arcmin-radius *i*-band frame (grey), masks around bright stars and outside the aperture of HE 0435−1223 (blue), and masks in the CFHTLenS fields (red) are depicted. Only the grey area which is not covered by any masks is used.

Table 2. Types of weights and weighted counts.

q	W_q^{sum}	W_q^{meds}
1	N_{gal}	N_{gal}
z	$\sum_{i=1}^{N_{\mathrm{gal}}} \left(z_{\mathrm{s}} \times z_i - z_i^2 \right)$	$N_{\mathrm{gal}} \times \mathrm{med} \left(z_{\mathrm{s}} \times z_i - z_i^2 \right)$
$M_\star^n$	$\sum_{i=1}^{N_{\mathrm{gal}}} M_{\star,i}^n$	$N_{\mathrm{gal}} \times \mathrm{med} \left(M_{\star,i}^n \right)$
$1/r$	$\sum_{i=1}^{N_{\mathrm{gal}}} 1/r_i$	$N_{\mathrm{gal}} \times \mathrm{med}(1/r_i)$
z/r	$\sum_{i=1}^{N_{\mathrm{gal}}} \left(z_{\mathrm{s}} \times z_i - z_i^2 \right) /r_i$	$N_{\mathrm{gal}} \times \mathrm{med} \left(z_{\mathrm{s}} \times z_i - z_i^2 \right) /r_i$
$M_\star^n/r$	$\sum_{i=1}^{N_{\mathrm{gal}}} M_{\star,i}^n/r_i$	$N_{\mathrm{gal}} \times \mathrm{med} \left(M_{\star,i}^n/r_i \right)$
$M_{\star,\mathrm{rms}}^n$	$\sqrt[n]{\sum_{i=1}^{N_{\mathrm{gal}}} M_{\star,i}^n}$	$\sqrt[n]{N_{\mathrm{gal}} \times \mathrm{med} \left(M_{\star,i}^n \right)}$
$M_\star^n/r_{,\mathrm{rms}}$	$\sqrt[n]{\sum_{i=1}^{N_{\mathrm{gal}}} M_{\star,i}^n/r_i}$	$\sqrt[n]{N_{\mathrm{gal}} \times \mathrm{med} \left(M_{\star,i}^n/r_i \right)}$
$M_\star/r^n$	$\sum_{i=1}^{N_{\mathrm{gal}}} M_{\star,i}/r_i^n$	$N_{\mathrm{gal}} \times \mathrm{med} \left(M_{\star,i}/r_i^n \right)$
$\sqrt{M_\star}/r$	$\sum_{i=1}^{N_{\mathrm{gal}}} \sqrt{M_{\star,i}}/r_i$	$N_{\mathrm{gal}} \times \mathrm{med} \left(\sqrt{M_{\star,i}}/r_i \right)$
$\sqrt{M_{\mathrm{h}}}/r$	$\sum_{i=1}^{N_{\mathrm{gal}}} \sqrt{M_{\mathrm{h},i}}/r_i$	$N_{\mathrm{gal}} \times \mathrm{med} \left(\sqrt{M_{\mathrm{h},i}}/r_i \right)$

Note. Here 'med' refers to the median, and $n = 1, 2, 3$ for weights not including 'rms' or r to powers larger than 1, $n = 2, 3$ otherwise.

the number of cells in a CFHTLenS field. Following the notation in G13, we generalize from number counts to weighted counts by replacing N_{gal} with $W_q = \sum_{i=1}^{N_{\mathrm{gal}}} q_i$, where q refers to a particular type of weight. Therefore ζ_{gal} generalizes to ζ_q.

Following G13 we adopt these weights: $q_{\mathrm{gal}} = 1$, i.e. simple galaxy counting; $q_{M_\star^n} = M_\star^n$ ($n = 1, 2, 3$), i.e. summing up powers of galaxy stellar masses; and $q_z = z_{\mathrm{s}} \times z - z^2$, i.e. weighting by redshift. In addition, we also consider weights incorporating the distance to the lens/centre of the field: $q_{1/r}$, $q_{M_\star^n/r}$, and $q_{z/r}$, as well as the weighted counts $W_{M_{\star,\mathrm{rms}}^n} = \sqrt[n]{\sum_{i=1}^{N_{\mathrm{gal}}} M_{\star,i}^n}$ and $W_{M_\star^n/r,\mathrm{rms}}$, ($n = 2, 3$).

In addition to the weights from G13, we define an additional weight, $M_\star/r^n$, where $n = 2, 3$ corresponds to the tidal and the flexion shift, respectively, of a point mass, as defined in McCully et al. (2017). We have simplified the definition of these two quantities by removing the explicit redshift dependence. This is because the lensing convergence maps of the MS are not designed to account for this dependence (Hilbert et al. 2009). Another weight, $\sqrt{M_\star}/r$, corresponds to the convergence produced by a singular isothermal sphere. We supplement this with a final related weight, $\sqrt{M_{\mathrm{h}}}/r$, where M_{h} stands for the halo mass of the galaxy, derived from the stellar mass by using the relation of Behroozi, Conroy & Wechsler (2010).

Finally, in addition to the summed weighted counts used by G13, we introduce an alternative type of weighted counts, which as we will later show, produces improved results. We refer to W_q defined above as W_q^{sum}, and we define $W_q^{\mathrm{meds}} = N_{\mathrm{gal}} \times \mathrm{median}(q_i)$, $i = 1, ..., N_{\mathrm{gal}}$. All of the weights and weighted counts defined above are summarized in Table 2. Separately from these, we will also use a supplementary constraint when selecting lines of sight from the MS: the shear value at the location of HE 0435−1223, $\gamma_{\mathrm{ext}} = 0.030 \pm 0.004$, as measured in H0LiCOW Paper IV for the fiducial lens model.

Following G13, we only consider galaxies of redshift $z < z_{\mathrm{s}}$. For $r \le 10$ arcsec we replace $1/r$ in all weights incorporating $1/r$ with $1/10$, in order to limit the contribution of the most nearby galaxies, which are accounted for explicitly in the mass model (paper IV). For the HE 0435−1223 field, where available, we use spectroscopic redshifts for every galaxy, and photometric redshifts for the rest. For CFHTLenS, we impose a bright magnitude cut of $i = 17.48$, corresponding to the brightest galaxy in the HE 0435−1223 field.

The final quantities that remain to be chosen are the aperture size and depth that we consider, both for the field around HE 0435−1223, and for CFHTLenS. Fassnacht et al. (2011) used a single aperture of 45 arcsec radius and galaxies down to 24 mag in F814W (Vega-based), mainly motivated by the size and depth of the *HST*/ACS chip used for their observations. G13 also adopted the same aperture and depth. Using their galaxy halo-model approach to reconstruct the mass distribution along the line of sight, Collett et al. (2013) determined using the MS that the majority of the κ_{ext} comes from galaxies inside an aperture of 2-arcmin-radius and brighter than $i = 24$ mag. Although our relative counts technique may reduce the sensitivity to the choice of aperture and depth, our observation campaigns were thus designed to reach $i = 24$ over a 2-arcmin-radius aperture, in light of the Collett et al. (2013) results.

Finally, in Fig. 4 we show the relative weight of each galaxy in the HE 0435−1223 field, where we mark our magnitude and aperture limits.

5.2 Resulting distributions for ζ_q

In this section we present our results, regarding the distribution of overdensities. The results are robust to different sources of systematic and random uncertainties, as we show in detail in Appendix B. The uncertainties discussed in the appendix include the choice of different aperture radii (45 and 120 arcsec) and limiting magnitudes ($i < 23$ and $i < 24$), using CFHTLenS cells with at least 75 or 50 per cent of their surface free of masks, considering the W1–W4 CFHTLenS individually in order to assess sample variance, and sampling from the inferred distribution of redshift and stellar mass for each galaxy.

We plot ζ_q^{WX}, $X = 1, 2, 3, 4$ for all weights q as well as a selection of aperture radii and limiting magnitudes, in Figs 5, B2 and B3.
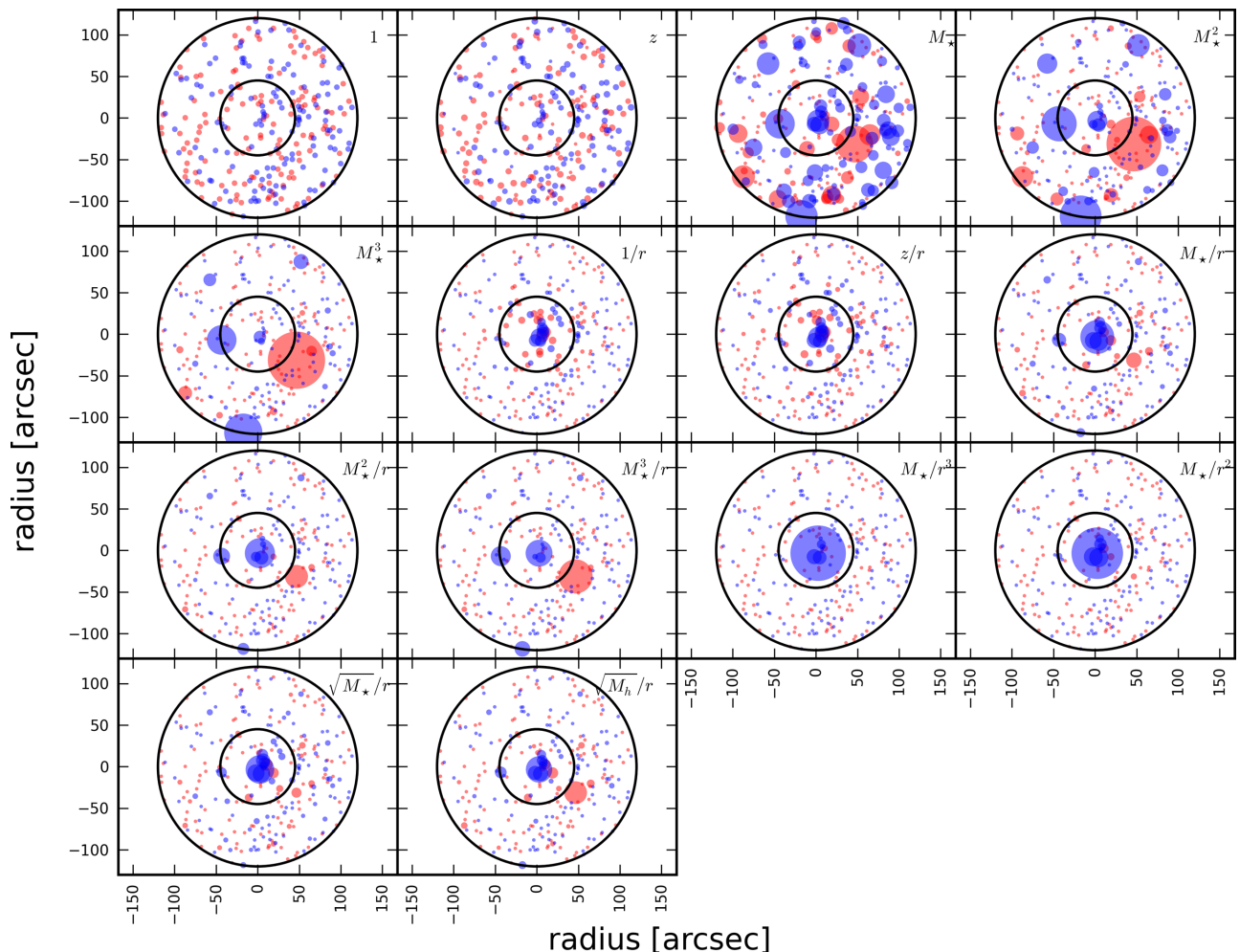
Figure 4. The relative weights of the galaxies around HE 0435−1223, represented by circles with areas proportional to their weights. Blue circles refer to $i \leq 23$ mag galaxies, whereas red circles refer to $23 < i < 24$ mag galaxies. A constant minimum circle radius is used for legibility.

These are known as ratio distributions, or, more approximately, inverse Gaussian distributions. There are two reasons why we take the medians of these distributions as an estimate of the field under/overdensity, $\overline{\zeta_q^{WX}} \equiv \text{median}\left(\zeta_q^{WX}\right)$, instead of the mean. First, because the median is robust to the long tails displayed by some of the distributions, whereas the use of means would imply that the field is of unphysically large overdensity. Secondly, so that we can use a numerical approximation which decreases significantly the computation time when estimating weighted count ratios in the MS (see Section C for details). This approach is much faster and more robust than clipped averages.

By comparing the ζ_q^{WX} distributions for different magnitude and aperture limits (Figs 5 and B2), it is apparent that the distributions corresponding to brighter limiting magnitude and smaller aperture are wider. This is due to larger Poisson noise when computing weighted counts, since fewer galaxies are included. In Figs 5 and B3 we show the distributions for ζ_q^{meds} and ζ_q^{sum}, respectively. ζ_q^{sum} shows more scatter between W1 and W4, and as we will show in Section 6, it is also more noisy. It also shows more clearly that fields W1 and W3 are relatively more similar to each other, and different from W2 and W4, as expected from the fact that these two latter fields have a larger fraction of star contaminants (see Section B). We find that distributions using cells with masked fractions

<50 per cent and <25 per cent are very similar, at ~1 per cent level. The scatter in $\zeta_q^{\text{meds},WX}$ for a given weight q (hereafter we only consider W1 and W3, given the result above) is also very small, indicating that sample variance in CFHTLenS is not an issue. The distributions are virtually unchanged if we compute stellar masses with or without the IRAC bands, and very similar whether EAZY or BPZ are used to compute redshifts. We find the largest differences when using different SEXTRACTOR detection parameters (in particular for the deeper magnitude limit of $i < 24$ mag), and when comparing the 10 distributions obtained from sampling from the redshift and stellar mass distributions of each galaxy (see Section B). In Table 3, we give the measured weighted ratios, where we include when computing the medians all the source of scatter discussed above.

Fig. 6 shows a radial plot of the measured overdensity for each weight, for four different aperture radii: 45 arcsec, 60 arcsec, 90 arcsec and 120 arcsec. The HE 0435−1223 field is comparatively more overdense for the brighter limiting magnitude ($i \leq 23$) and, at the brighter limiting magnitude, for the 45 arcsec aperture.

We note that the 1.27 ± 0.05 unweighted count overdensity we measure inside 45 arcsec, for $i \leq 24$, is larger than the underdensity of 0.89 (± 0.12, assuming simple Poisson noise), measured by Fassnacht et al. (2011) inside the same aperture. This
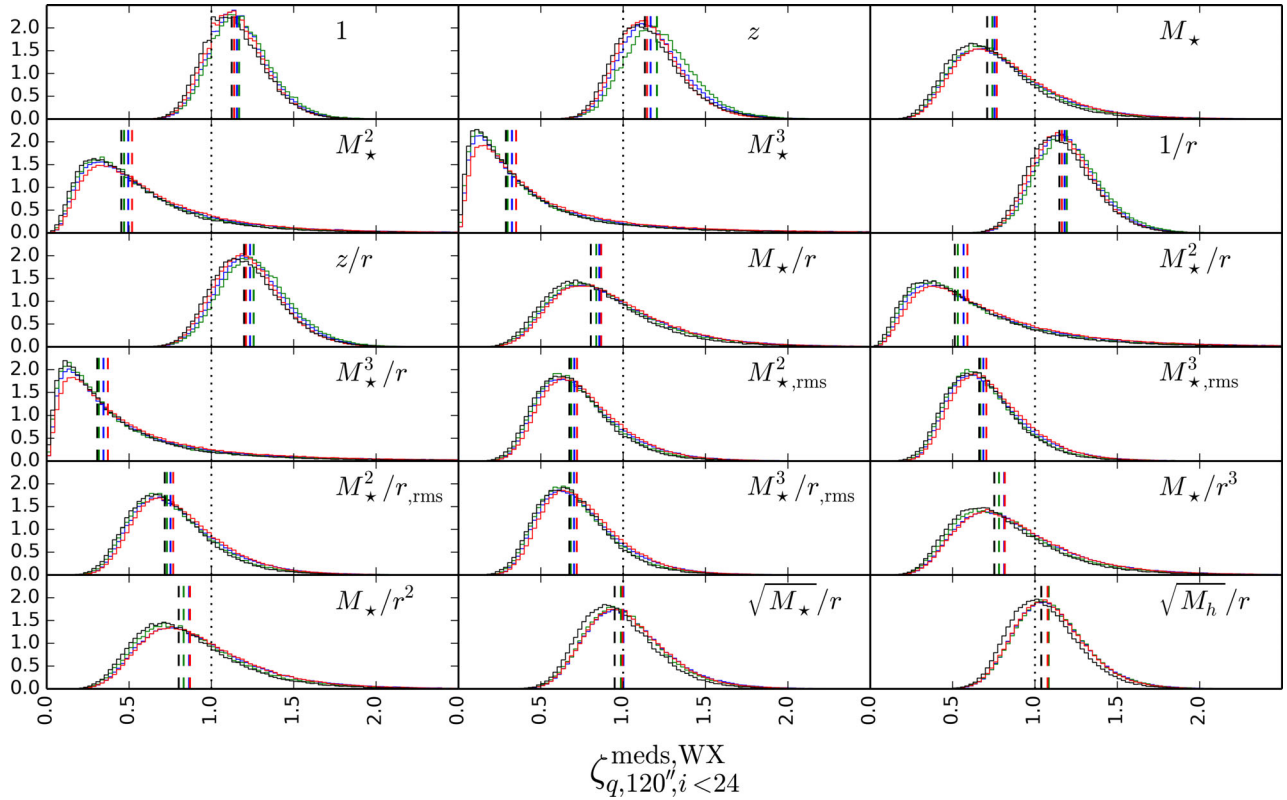
Figure 5. Normalized histograms of weighted ratios for all $\zeta_q^{\mathrm{meds,WX}}$ weights, where $X = 1$ (blue), $X = 2$ (green), $X = 3$ (red), $X = 4$ (black), for galaxies inside a 120-arcsec-radius aperture and $i \leq 24$. We only plot the distributions obtained from using CFHTLenS apertures with at least 75 per cent of their surface free of masks, as the 75 per cent–50 per cent limit distributions appear virtually identical. The vertical dashed lines mark the medians of the distributions.

**Table 3.** Weighted galaxy count ratios $\overline{\zeta_q}$ for HE 0435−1223.

Weight q	45 arcsec $i < 24$ sum	45 arcsec $i < 24$ meds	45 arcsec $i < 23$ sum	45 arcsec $i < 23$ meds	120 arcsec $i < 24$ sum	120 arcsec $i < 24$ meds	120 arcsec $i < 23$ sum	120 arcsec $i < 23$ meds
1	1.27 ± 0.05	1.27 ± 0.05	1.35 ± 0.04	1.35 ± 0.04	1.15 ± 0.04	1.15 ± 0.04	1.23 ± 0.03	1.23 ± 0.03
z	1.25 ± 0.05	1.20 ± 0.05	1.43 ± 0.04	1.31 ± 0.03	1.20 ± 0.04	1.16 ± 0.04	1.27 ± 0.03	1.21 ± 0.03
$M_\star$	0.88 ± 0.03	0.66 ± 0.10	1.23 ± 0.05	2.01 ± 0.17	0.61 ± 0.03	0.76 ± 0.04	0.71 ± 0.05	0.97 ± 0.08
$M_\star^2$	0.70 ± 0.09	0.34 ± 0.12	1.17 ± 0.16	2.95 ± 0.45	0.24 ± 0.13	0.51 ± 0.06	0.32 ± 0.19	0.76 ± 0.14
$M_\star^3$	0.67 ± 0.17	0.18 ± 0.10	1.38 ± 0.35	4.3 ± 1.0	0.11 ± 0.26	0.34 ± 0.06	0.16 ± 0.40	0.60 ± 0.15
$1/r$	1.47 ± 0.05	1.31 ± 0.05	1.71 ± 0.03	1.30 ± 0.02	1.25 ± 0.04	1.17 ± 0.04	1.40 ± 0.02	1.27 ± 0.02
z/r	1.52 ± 0.06	1.17 ± 0.05	1.90 ± 0.04	1.26 ± 0.05	1.30 ± 0.04	1.22 ± 0.05	1.47 ± 0.06	1.33 ± 0.03
$M_\star/r$	1.25 ± 0.04	0.61 ± 0.05	1.77 ± 0.06	2.03 ± 0.19	0.74 ± 0.03	0.86 ± 0.05	0.92 ± 0.04	1.06 ± 0.07
$M_\star^2/r$	0.76 ± 0.07	0.35 ± 0.06	1.28 ± 0.12	3.1 ± 0.7	0.28 ± 0.08	0.58 ± 0.05	0.38 ± 0.11	0.76 ± 0.11
$M_\star^3/r$	0.56 ± 0.11	0.16 ± 0.08	1.15 ± 0.20	4.7 ± 1.6	0.11 ± 0.15	0.36 ± 0.06	0.17 ± 0.24	0.57 ± 0.11
$M_{\star,\mathrm{rms}}^2$	0.84 ± 0.05	0.59 ± 0.09	1.08 ± 0.07	1.72 ± 0.14	0.49 ± 0.11	0.71 ± 0.04	0.57 ± 0.13	0.87 ± 0.08
$M_{\star,\mathrm{rms}}^3$	0.87 ± 0.07	0.56 ± 0.09	1.11 ± 0.09	1.62 ± 0.13	0.48 ± 0.18	0.70 ± 0.04	0.55 ± 0.22	0.84 ± 0.07
$M_\star^2/r_{,\mathrm{rms}}$	0.87 ± 0.04	0.59 ± 0.05	1.13 ± 0.05	1.75 ± 0.20	0.53 ± 0.06	0.76 ± 0.04	0.62 ± 0.08	0.88 ± 0.06
$M_\star^3/r_{,\mathrm{rms}}$	0.82 ± 0.05	0.54 ± 0.07	1.05 ± 0.07	1.68 ± 0.18	0.48 ± 0.13	0.71 ± 0.04	0.56 ± 0.15	0.83 ± 0.05
$M_\star/r^3$	3.8 ± 0.2	0.56 ± 0.08	6.2 ± 0.3	1.8 ± 0.3	3.25 ± 0.16	0.82 ± 0.09	5.05 ± 0.25	1.31 ± 0.13
$M_\star/r^2$	2.2 ± 0.1	0.61 ± 0.08	3.25 ± 0.15	2.07 ± 0.25	1.46 ± 0.06	0.87 ± 0.05	2.02 ± 0.09	1.21 ± 0.08
$\sqrt{M_\star}/r$	1.46 ± 0.03	0.89 ± 0.06	2.00 ± 0.04	1.68 ± 0.10	1.05 ± 0.02	1.00 ± 0.04	1.26 ± 0.02	1.23 ± 0.04
$\sqrt{M_\mathrm{h}}/r$	1.18 ± 0.02	1.01 ± 0.05	1.67 ± 0.04	1.42 ± 0.07	0.76 ± 0.04	1.08 ± 0.04	0.92 ± 0.06	1.21 ± 0.04

Notes. Medians of weighted galaxy counts for HE 0435−1223, inside various aperture radii and limiting magnitudes. The errors include, in quadrature, scatter from 10 samplings of redshift and stellar mass for each galaxy in HE 0435−1223, scatter from W1 and W3, BPZ–EAZY, and two different SEXTRACTOR detections.

is likely due to the deeper magnitude limit they used, their much smaller control field, as well as possibly the use of a less careful masking technique. The present result supersedes the earlier analysis.

5.3 Computing simulated ζ_q in the MS

Here, we compute weighted count ratios ζ_q from simulated fields obtained from the MS (Springel et al. 2005), trying to closely reproduce the data quality of the HE 0435−1223 and the CFHTLenS
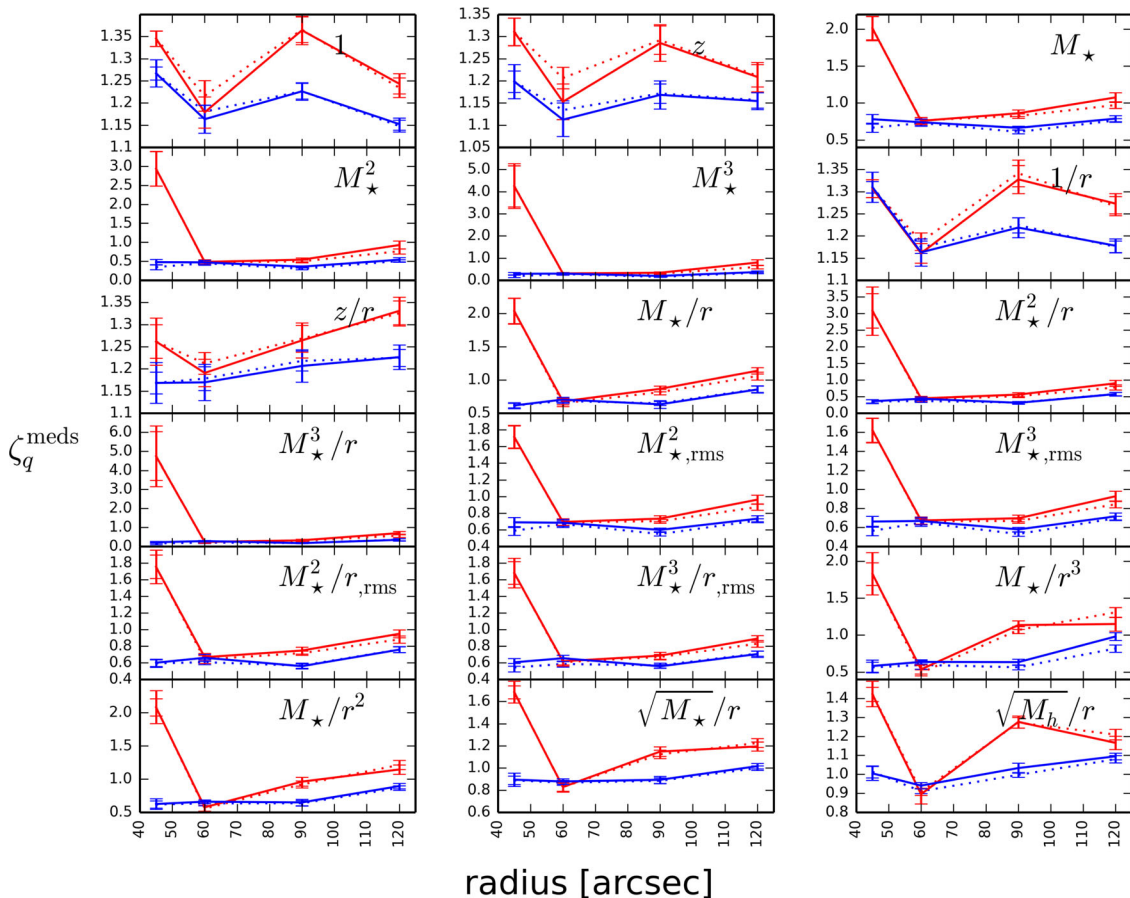
Figure 6. Radial plot of the measured weighted count ratios ζ_q^{meds}, calculated for aperture radii of 45 arcsec, 60 arcsec, 90 arcsec and 120 arcsec, using the combined CFHTLenS W1 and W3 fields. The blue line refers to $i \leq 24$, and the red line to $i \leq 23$. The solid line refers to redshifts estimated with BPZ, and the dotted line refers to redshifts determined with EAZY. The ranges of the vertical axes are different. Error bars include the scatter between W1 and W4, and sampling from the galaxy magnitudes, redshifts and stellar masses (see text). They do not include scatter between different SExtractor parameters, which are included in Table 3.

fields. We do this for two main reasons: first, since we will infer $P(\kappa_{\mathrm{ext}})$ by selecting lines of sight of specific overdensities from the MS, we need to ensure that it is fair to compare the overdensities in the MS to those in the real data. Secondly, by using the MS we can compare the overdensities we measure with their 'true' values, and thus assess the quality of our estimates.

The MS is an *N*-body simulation of cosmic structure formation in a cubic region ∼680 Mpc of comoving size, with a halo mass resolution of 2×10^{10} M$_\odot$ (corresponding approximately to a galaxy with luminosity $0.1L_\star$). Catalogues of galaxies populating the matter structures in the simulation were generated based on the semi-analytic galaxy models by De Lucia & Blaizot (2007), Guo et al. (2011) and Bower et al. (2006). Furthermore, 64 simulated fields of 4×4 deg^2 were produced from the MS by ray-tracing (Hilbert et al. 2009). These simulated fields contain, among other information, the observed positions, redshifts, stellar masses and apparent magnitudes (e.g. in the SDSS *ugriz* and 2MASS *JHK$_s$* filters) of the galaxies in the field, as well as the gravitational lensing convergence κ_{ext} and shear γ_{ext} as a function of image position and source redshifts.

We use each of the MS fields, in turn, as fields whose overdensities we want to measure ('HE 0435−1223-like fields'), as well as fields against which we measure those overdensities ('control fields'). For the HE 0435−1223 like fields we consider only their

ugriJHK$_s$ photometry, whereas for the calibration fields we use their *ugriz* photometry. Based on these, we compute photometric redshifts and stellar masses for all ∼70 million $i < 24$ mag galaxies, using the same techniques we employed for the real data. This is because the stellar masses and redshifts in our real data suffer from observational uncertainties, which are not present in the available synthetic catalogues. For each galaxy, we randomly sample its 'observed' magnitude in a given band from a Gaussian around its catalogue magnitude, with a standard deviation given by the typical photometric uncertainty of galaxies of similar magnitude in the real data. In Fig. 7 we compare the redshifts and stellar masses estimated for the galaxies in the MS with the catalogue values, using photometry based on the De Lucia & Blaizot (2007) semi-analytic models. We find better results compared to the catalogues based on Guo et al. (2011) and Bower et al. (2006), and therefore we use the De Lucia & Blaizot (2007)-based catalogue throughout this work. The photometric redshift bias, scatter and fraction of outliers are generally comparable to the ones measured for CFHTLenS and HE 0435−1223 field galaxies, the only exception being that the fraction of outliers measured for CFHTLenS is larger (15 per cent compared to 2 per cent). We stress here that the superiority of the De Lucia & Blaizot (2007) semi-analytic models is likely a consequence of these models being more similar to the templates used by BPZ and LE PHARE. However, we are only interested in the
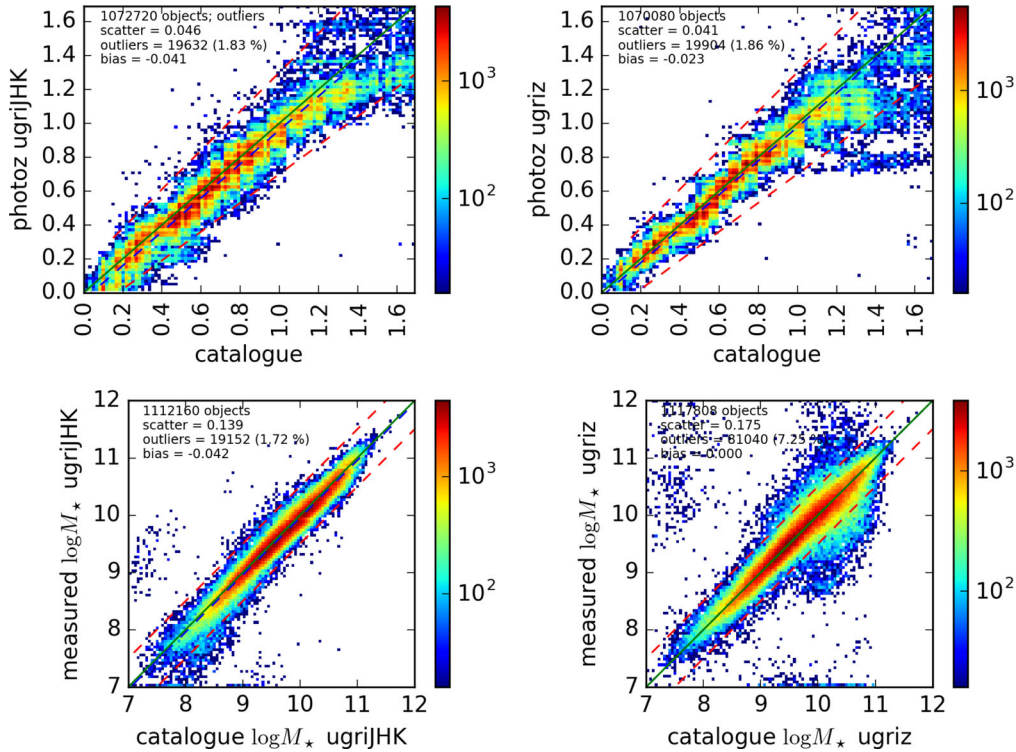
Figure 7. Performance of the photometric redshift and stellar mass estimation in the MS, using the mock galaxy catalogue based on the De Lucia & Blaizot (2007) semi-analytic models, for galaxies inside a $4 \times 4 \ \mathrm{deg}^2$ field. Two different combinations of filters are used, as well as simulated photometric errors representative of the HE 0435−1223 and CFHTLenS data. The bias for the photometric redshift when only $z < 1$ objects are included decreases to -0.029 and -0.011 for the $ugriJHK_s$ and the $ugriz$ bands, respectively. For the lower plots, we define the outliers as $|\Delta \log M_\star| > 0.5$.

empirical result that by using these models we obtain similar uncertainties in the simulations, and in the real data. We thus conclude that we can indeed use the MS galaxy catalogue to estimate overdensities with uncertainties similar to those found in the real data.

We consider the same apertures and limiting magnitudes we used in the real data. In addition, we use the fact that a specific fraction of galaxies in the real HE 0435−1223 field have spectroscopic redshift, as a function of magnitude and aperture radius. For these galaxies, we use their 'true', catalogue redshifts. We calculate stellar masses with LE PHARE, in the same way we did for the real data, in particular using the same templates. There are, however, several differences to our approach, compared to the real data, which we present in Appendix C.

Next, we test how the 'measured' overdensities compare to 'true' overdensities, obtained by using the 'true' values of redshift and stellar mass for each galaxy, readily available in the catalogue for the whole MS. We show the comparisons for $\zeta_q^{i\in\mathrm{MS,sum}}$ and $\zeta_q^{i\in\mathrm{MS,meds}}$ in Figs 8 and 9, respectively. $\zeta_q^{i\in\mathrm{MS,sum}}$ is a much noisier estimate than $\zeta_q^{i\in\mathrm{MS,meds}}$, and this is particularly obvious for all weights incorporating stellar mass, due to the high dynamic range of this quantity. This justifies our definition of $\zeta_q^{i\in\mathrm{MS,meds}}$ as a better estimate.

We have also checked that a larger aperture radius and fainter magnitude limit produce smaller scatter, which is expected because they include more galaxies, resulting in less Poisson noise; the improvement is much more dependent on radius than on magnitude.

Finally, in Fig. 10 we show the relations between the different ζ_q. We find that the different ζ_q are correlated, as expected from their definitions, and that the specific values we determined for the HE 0435−1223 field are realistic in the sense that they are expected at $\sim$1–2 σ. We have checked that this result is robust to changing the aperture radius and limiting magnitude.

By this point, we have related the κ_ext^i points (centres of each cell) in the 64 fields of the MS, where i refers to each available cell, to their corresponding $\zeta_q^{i\in\mathrm{MS,meds}}$. In addition, we have also recorded the corresponding values of the shear $\gamma_\mathrm{ext}{}^i$, to use as an additional constraint. H0LiCOW Paper IV measured a constant external shear strength (in addition to the shear stemming from explicit mass models of the strong-lens and nearby galaxies), which is close to the median of the shear distribution through the MS. This is helpful for ruling out high values from the κ_ext distribution (see fig. 8 in Collett & Cunnington 2016). Our use of all available κ_ext^i points in the MS (most of which are not strong-lensing lines of sight) is justified by Hilbert et al. (2009) and Suyu et al. (2010), which showed that the distribution of κ_ext from lines of sight to a strong lens is very similar to, and can be approximated by, the distribution for normal lines of sight (i.e. without a strong lens). We note that the redshift of the source quasar in HE 0435−1223, $z = 1.69$, lies between two redshift planes in the MS, at $z = 1.63$ and $z = 1.77$. We therefore adopted the mean of the two planes for each value of the convergence κ_ext and shear γ_ext.[7]

6 DETERMINING $P(\kappa_\mathrm{ext})$

In the previous sections, we have explained how we estimate weighted count ratios for the real data, and analogously for the MS, and we have related every κ_ext point in the MS to the corresponding weighted count ratio around its line of sight. We now

---

[7] While there are noticeable differences between individual values, we have determined $P(\kappa_\mathrm{ext})$ separately for a single plane, and found that the impact on the distribution is negligible, as the median of inferred $P(\kappa_\mathrm{ext})$ changes by only $\sim$0.002 if we assume the source is at $z = 1.63$.
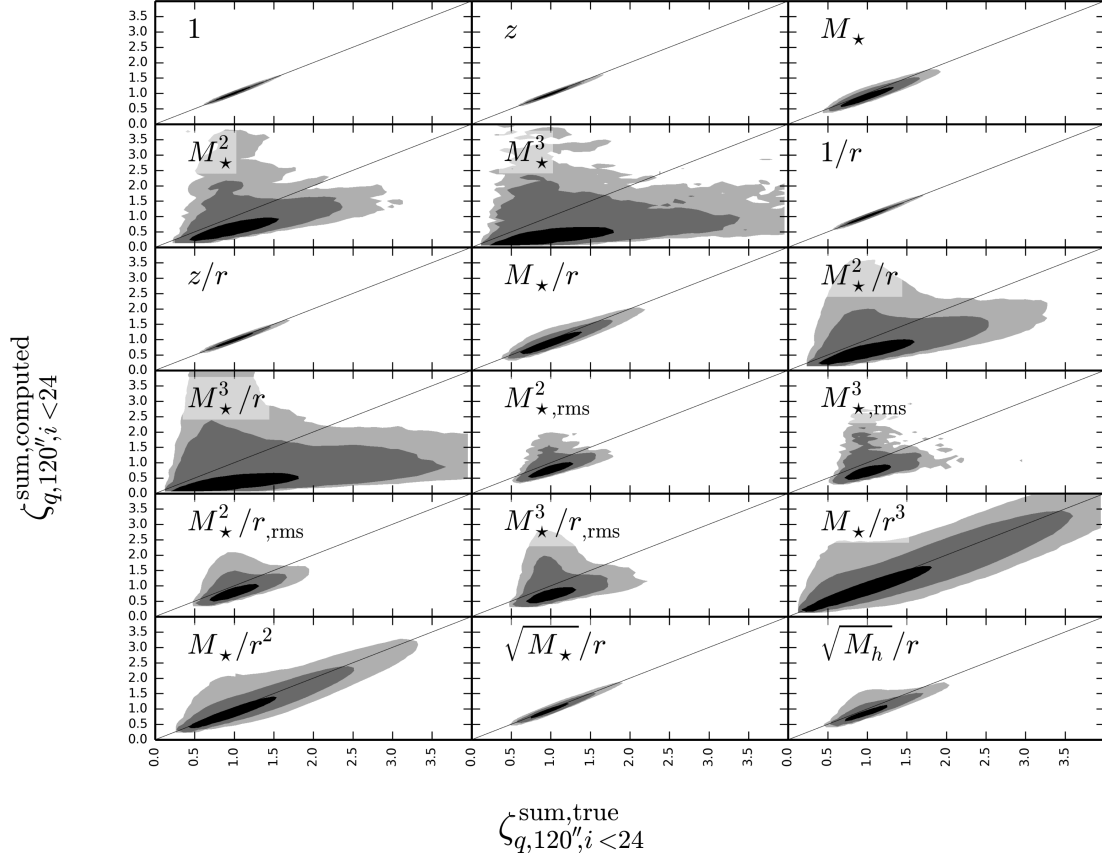
Figure 8. Catalogue versus computed weighted ratios from the MS, using the mock galaxy catalogue based on the De Lucia & Blaizot (2007) semi-analytic models, for galaxies inside a 4×4 deg^2 field. Each point represents $\zeta_q^{i \in \text{MS,sum}}$ for 120-arcsec radius, $i \leq 24$ mag. Black, dark and light grey filled contours encompass regions of 1σ, 2σ and 3σ, respectively. The black line represents the diagonal.

present the mathematical formalism and implementation necessary to obtain the distribution of κ_{ext} given our knowledge of weighted count ratios around HE 0435−1223.

6.1 Theory and implementation

We aim to estimate $P(\kappa_{\text{ext}})$ using the MS catalogue of κ_{ext} points, in a fully Bayesian framework. By $P(\kappa_{\text{ext}})$ we refer to $p(\kappa_{\text{ext}}|\boldsymbol{d})$, where $\boldsymbol{d}$ stands for the available data, and we have made our dependence on the data explicit. The data refer to our catalogue of galaxies inside a given aperture and magnitude threshold, for both the HE 0435−1223 and the CFHTLenS fields. It includes the galaxy number, galaxy positions in their respective apertures, as well as redshifts and stellar masses. In the sections given above, we used these data in order to infer $\overline{\zeta_q^{\text{WX}}}$, which we denote below as ζ_q, and is by construction a noisy quantity. We use ζ_q as a random variable, whose connection to the data and the external convergence can be expressed by a joint distribution $p(\kappa_{\text{ext}}, \zeta_q, \boldsymbol{d})$. Then, $p(\kappa_{\text{ext}}|\boldsymbol{d})$ can be expressed as:

$$p(\kappa_{\text{ext}}|\boldsymbol{d}) = \frac{p(\kappa_{\text{ext}}, \boldsymbol{d})}{p(\boldsymbol{d})} = \int \mathrm{d}\zeta_q \frac{p(\kappa_{\text{ext}}, \zeta_q, \boldsymbol{d})}{p(\boldsymbol{d})}. \quad (4)$$

Next, we make the assumption that

$$p(\boldsymbol{d}|\kappa_{\text{ext}}, \zeta_q) = p(\boldsymbol{d}|\zeta_q), \quad (5)$$

i.e. the likelihood of the data does not explicitly depend on the external convergence, for fixed ζ_q. This is justified, since we have defined ζ_q based solely on the data, without reference to the external

convergence. From this,

$$p(\kappa_{\text{ext}}, \zeta_q, \boldsymbol{d}) = p(\kappa_{\text{ext}}, \zeta_q)p(\boldsymbol{d}|\kappa_{\text{ext}}, \zeta_q)$$

$$= p(\kappa_{\text{ext}}, \zeta_q)p(\boldsymbol{d}|\zeta_q) = p(\kappa_{\text{ext}}, \zeta_q)\frac{p(\zeta_q, \boldsymbol{d})}{p(\zeta_q)}, \quad (6)$$
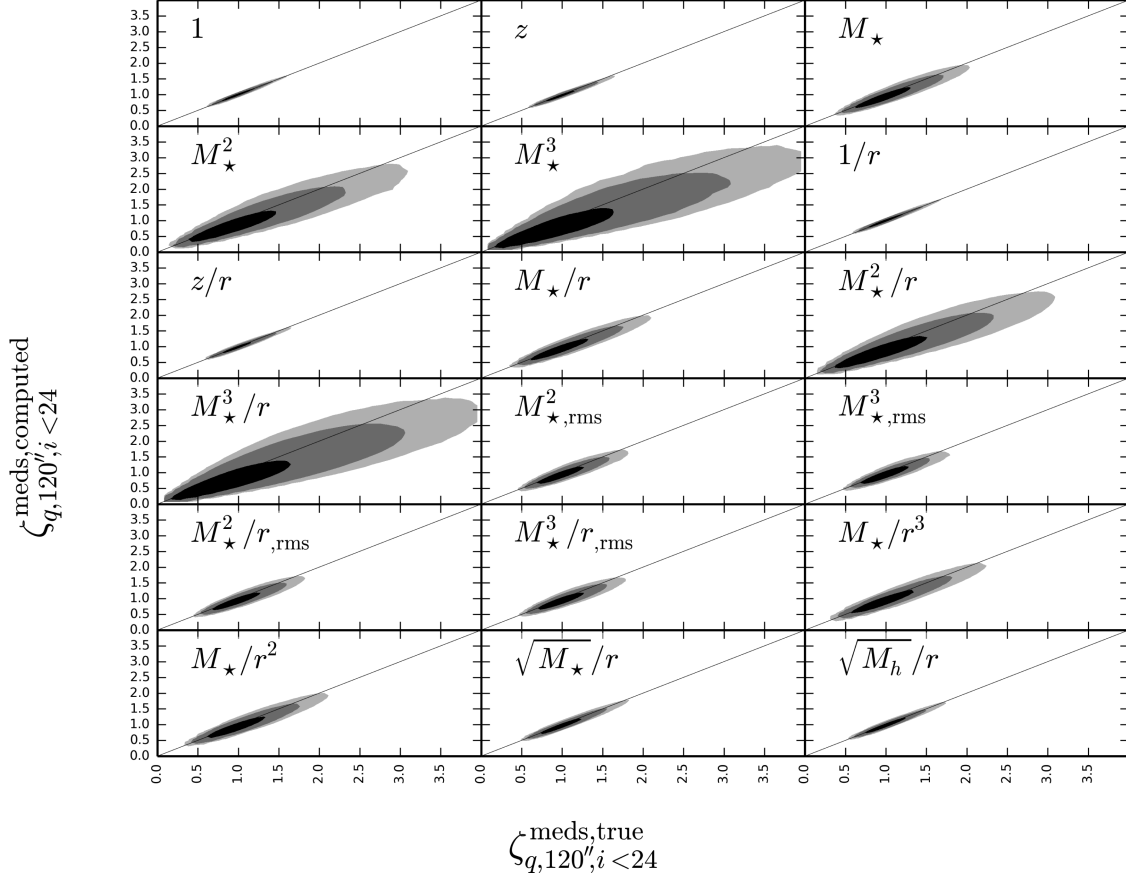
and thus

$$p(\kappa_{\text{ext}}|\boldsymbol{d}) = \int \mathrm{d}\zeta_q \frac{p(\kappa_{\text{ext}}, \zeta_q)p(\zeta_q, \boldsymbol{d})}{p(\zeta_q)p(\boldsymbol{d})}$$

$$= \int \mathrm{d}\zeta_q\, p(\kappa_{\text{ext}}|\zeta_q)p(\zeta_q|\boldsymbol{d}). \quad (7)$$

That is, given our estimate of ζ_q from the data, by using a correspondence between ζ_q and κ_{ext}, we obtain the κ_{ext} distribution. Here, we consider $p(\zeta_q|\boldsymbol{d}) \equiv N_q\left(\zeta_q; \sigma_{\zeta_q}\right)$ to be a Gaussian with mean and standard deviation given in Table 3, and we make use of the MS by replacing $p(\kappa_{\text{ext}}|\zeta_q)$ with $p_{\text{MS}}(\kappa_{\text{ext}}|\zeta_q^{\text{MS,meds}} \equiv \zeta_q)$.

As mentioned in Section 1, G13 showed that the standard deviation of $P(\zeta_q|\boldsymbol{d})$, which we denote as σ_κ, can decrease when information is added by using multiple conjoined weights. They found the best improvement when using combinations of three weights, including q_{gal} and $q_{1/r}$. We make use of this result, and consider a third weight from those in Section 5.1, in addition to the shear constraint. Thus, our distribution becomes

$$p(\kappa_{\text{ext}}|\boldsymbol{d}) = \int \mathrm{d}\zeta_1\, d\zeta_{1/r} d\zeta_{q \neq 1, 1/r} d\zeta_{\gamma\text{ext}} p_{\text{MS}}(\kappa_{\text{ext}}|\zeta_1, \zeta_{1/r},$$

$$...\zeta_{q \neq 1, 1/r}, \zeta_{\gamma\text{ext}})p(\zeta_1, \zeta_{1/r}, \zeta_{q \neq 1, 1/r}, \zeta_{\gamma\text{ext}}|\boldsymbol{d}). \quad (8)$$

Figure 9. Same as Fig. 8, but for $\zeta_q^{i \in \mathrm{MS,meds}}$.

We determined $p(\zeta_q|\boldsymbol{d})$ from the data independently for each q as Gaussians much narrower than the distributions whose medians they represent (e.g. Figs 5 and B2). We can thus factorize

$$p(\zeta_1, \zeta_{1/r}, \zeta_{q \neq 1,1/r}, \zeta_{\gamma \mathrm{ext}}|\boldsymbol{d})$$
$$\simeq p(\zeta_1|\boldsymbol{d})p(\zeta_{1/r}|\boldsymbol{d})p(\zeta_{q \neq 1,1/r}|\boldsymbol{d})p(\zeta_{\gamma \mathrm{ext}})|\boldsymbol{d}). \quad (9)$$

We remind the reader that in general (i.e. over the whole extent of their distribution) the ζ_q are correlated, as we have seen in Section 5.3, and not independent.[8]

G13 showed that simply adding up κ_{ext} points corresponding to lines of sight with $N_{\mathrm{gal}} \in \zeta_{q_{\mathrm{gal}}} \overline{N}_{\mathrm{gal}} \pm \mathrm{E}_{q_{\mathrm{gal}}}$ (this generalizes to $(W_q/\overline{W}_q)\overline{N}_{\mathrm{gal}} \in \zeta_q \overline{N}_{\mathrm{gal}} \pm \mathrm{E}_q)$ would bias $P(\kappa_{\mathrm{ext}})$. Here $\overline{N}_{\mathrm{gal}}$ is the median number of galaxies in an aperture of interest around a given line of sight from the MS, and E_q we choose to be twice the width of $p(\zeta_q|\boldsymbol{d})$. The bias comes from the fact that, e.g. for a relatively overdense field, the number of lines of sight N_{LOS} available with a galaxy count N_{gal} will be larger than that with a galaxy count $N_{\mathrm{gal}} + 1$ (i.e. there are comparatively fewer fields more overdense than a field which is already overdense). A larger number of lines of sight means that their respective κ_{ext} distribution will be over-represented, and the overall $P(\kappa_{\mathrm{ext}})$ will be biased towards those values. The solution adopted by G13 is to divide the $2\mathrm{E}_q$ interval

into $2\mathrm{E}_q$ bins of individual length 1[9] (for $\zeta_{q_{\mathrm{gal}}} = 1$ this corresponds to incrementing $\overline{N}_{\mathrm{gal}}$ by 1), and weight the κ_{ext} distribution in each of the bins by $1/N_{\mathrm{LOS}}$, where N_{LOS} is the number of lines of sight in that particular bin. This way, each of the $2\mathrm{E}_q$ κ_{ext} distributions carries equal weight into the combined distribution. In our case, we typically use four conjoined constraints $\{q_i, q_j, q_k, q_l\} = \{q_{\mathrm{gal}}, q_{1/r}, q \neq \{1, 1/r\}, q_{\gamma \mathrm{ext}}\}$, and therefore have $2\mathrm{E}_{q_i} \times 2\mathrm{E}_{q_j} \times 2\mathrm{E}_{q_h} \times 2\mathrm{E}_{q_k}$ multidimensional bins.

We account for the bias discussed above and compute $p(\kappa_{\mathrm{ext}}|\boldsymbol{d})$ as a series of nested sums

$$\sum_{i \in}^{\zeta_{q_i} \overline{N}_{\mathrm{gal}} \pm \mathrm{E}_i} \sum_{j \in}^{\zeta_{q_j} \overline{N}_{\mathrm{gal}} \pm \mathrm{E}_j} \sum_{k \in}^{\zeta_{q_k} \overline{N}_{\mathrm{gal}} \pm \mathrm{E}_k} \sum_{l \in}^{\zeta_{q_l} \overline{N}_{\mathrm{gal}} \pm \mathrm{E}_l} p_{\mathrm{MS}}(\kappa_{\mathrm{ext}}|\zeta_{q_i},$$
$$\ldots \zeta_{q_j}, \zeta_{q_k}, \zeta_{q_l}) \frac{\prod_{x=i,j,k,l} N_x \left(\zeta_{q_x}; \sigma_{\zeta_{q_x}}\right)}{N_{\mathrm{LOS}}^{(i,j,k,l)}}, \quad (10)$$

where $N_{\mathrm{LOS}}^{(i,j,k,l)}$ is the number of lines of sight in each multidimensional bin with indices (i, j, k, l), and p_{MS} is the distribution of κ_{ext} corresponding to each of these lines of sight.

For brevity, we refer to $p(\kappa_{\mathrm{ext}}|\boldsymbol{d})$ implemented by equation (10) as $P(\kappa_{\mathrm{ext}}|\zeta_1, \zeta_{1/r}, \zeta_{q \neq 1, 1/r}, \zeta_{\gamma \mathrm{ext}})$. We also consider selected distributions with fewer constraints. There are two practical limitations in not using more than four conjoined constraints. First, applying

---

[8] We tested that the approximation in equation (9) is justified by measuring the correlation coefficients between ζ_1, $\zeta_{1/r}$, and $\zeta_{q \neq 1,1/r}$ to be ~ 0 (at most ~ 0.2, in rare cases), for the relevant narrow range of interest.

[9] In practice, in order to reduce dimensionality, we allow the bins to be as large as 2. G13 (see their fig. 1) showed that this introduces negligible differences.
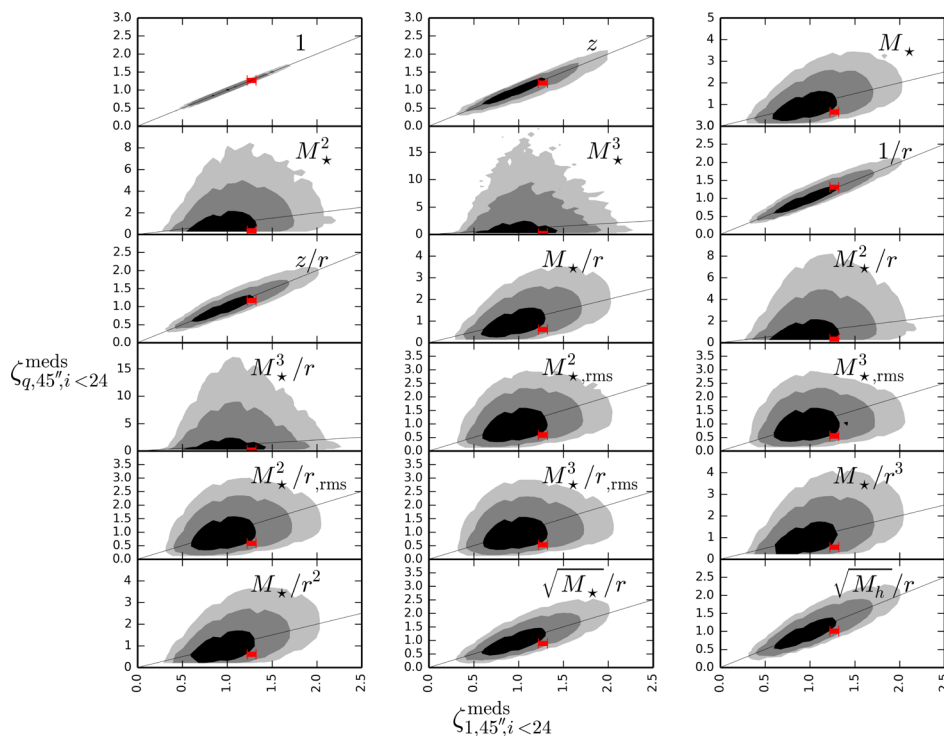
Figure 10. Relation between number count ratios ζ_1 and weighted number count ratios ζ_q, from the MS, using observational uncertainties similar to those of the HE 0435−1223 field. The cells inside a 4×4 deg^2 simulated field were used to construct the plot. The black, dark grey and light grey regions surround the 1-, 2- and 3-σ intervals, respectively. The black line represents the diagonal. The red error bars mark the measured overdensities for HE 0435−1223, and the associated 1-σ error bars.

equation (10) is computationally intensive, and scales quickly with the number of dimensions. Secondly, the MS contains a limited number of κ points, and the number of such points included in a bin decreases as additional constraints are added.

6.2 Testing for biases using simulated data

It is possible to use the MS itself to estimate the accuracy of our $p(\kappa_{\rm ext}|\boldsymbol{d})$ estimation, and test for biases. First, we randomly select 5000 cells from the MS, which are similar in terms of overdensity to HE 0435−1223. We then estimate $p(\kappa_{\rm ext}|\boldsymbol{d})$ for each of them. However, since this estimation would be computationally expensive, we consider very small uncertainties around the computed overdensities, so that equation (10) reduces to the computation of a single distribution, in one bin. For each of the 5000 distributions, we record its median, $\kappa_{\rm ext}^{\rm med}$. We then determine the distribution of $\kappa_{\rm ext}^{\rm med} - \kappa_{\rm ext}^{\rm true}$, where $\kappa_{\rm ext}^{\rm true}$ is the true value at the centre of each cell. We plot in Fig. 11 the median and standard deviation of this distribution, for each weight combination, as well as aperture radius and limiting magnitude. We find that $\kappa_{\rm ext}^{\rm med}$ is typically an unbiased estimate of $\kappa_{\rm ext}^{\rm true}$, to better than $\lesssim 0.0025$. In the 45 arcsec aperture $\kappa_{\rm ext}^{\rm med}$ seems to slightly overestimate $\kappa_{\rm ext}^{\rm true}$, whereas in the 120 arcsec aperture there is the opposite tendency. These estimates are noisy, with a standard deviation of ~0.020–0.025. This is to be expected: being the median of a distribution of $\kappa_{\rm ext}^{\rm true}$ values, $\kappa_{\rm ext}^{\rm med}$ cannot vary too much, compared to the individual $\kappa_{\rm ext}^{\rm true}$ points. However, the standard deviations of the 5000 individual distributions are also ~0.025, which means that $\kappa_{\rm ext}^{\rm true}$ is typically well-contained inside the individual distributions.

Next, we follow the example of Collett et al. (2013) in assessing the presence of biases in our estimation of the full $p(\kappa_{\rm ext}|\boldsymbol{d})$ distribu-

tion. In the absence of biases, $p(\kappa_{\rm ext} - \kappa_{\rm ext}^{\rm true}|\boldsymbol{d})$ is centred on zero. For different cells, these offset distributions can be multiplied together, resulting in a narrower distribution $P_N = \prod_{i=1}^{N} p_i(\kappa_{\rm ext} - \kappa_{\rm ext}^{\rm true}|\boldsymbol{d})$. Offsets from zero in the centroid of this distribution would be indicative of biases. We show the results of this approach in Fig. 12, where we adopt $N = 100$, and find no indication of offsets for any of the weights we consider. We conclude that, for fields of overdensity similar to HE 0435−1223, our technique is not affected by biases.

7 RESULTS AND DISCUSSION

We first present the results on the distribution of external convergence in Fig. 13. The HE 0435−1223 field is slightly overdense in terms of unweighted galaxy counts for aperture radius 45 arcsec, $i < 24$ mag, and therefore $P(\kappa_{\rm ext}|\zeta_{q_{\rm gal}})$ results in a more positive $\kappa_{\rm ext}^{\rm med}$ of 0.006, compared to −0.010 in the case that no constraints are used. The addition of the radial dependence constraint, $P(\kappa_{\rm ext}|\zeta_{q_{\rm gal}}, \zeta_{q_{1/r}})$, in terms of which the field is slightly more overdense, moves the distribution further to slightly more positive $\kappa_{\rm ext}^{\rm med}$. On the other hand, since the measured shear is similar to the median one through the MS, adding the shear constraint $P(\kappa_{\rm ext}|\zeta_{q_{\rm gal}}, \zeta_{q_{1/r}}, \zeta_{\gamma\rm ext})$ has the effect of narrowing the distribution, and moving it back towards lower $\kappa_{\rm ext}^{\rm med}$ of 0.004.

We show the resulting medians and standard deviations of the distributions for all weight combinations, as well as aperture radii and limiting magnitudes, in Fig. 14, and summarize the results in Table 4 . We find that the addition of weighted count constraints, on top of the constraints from shear, unweighted number counts and distance to the lens, only moves the peak and width of the
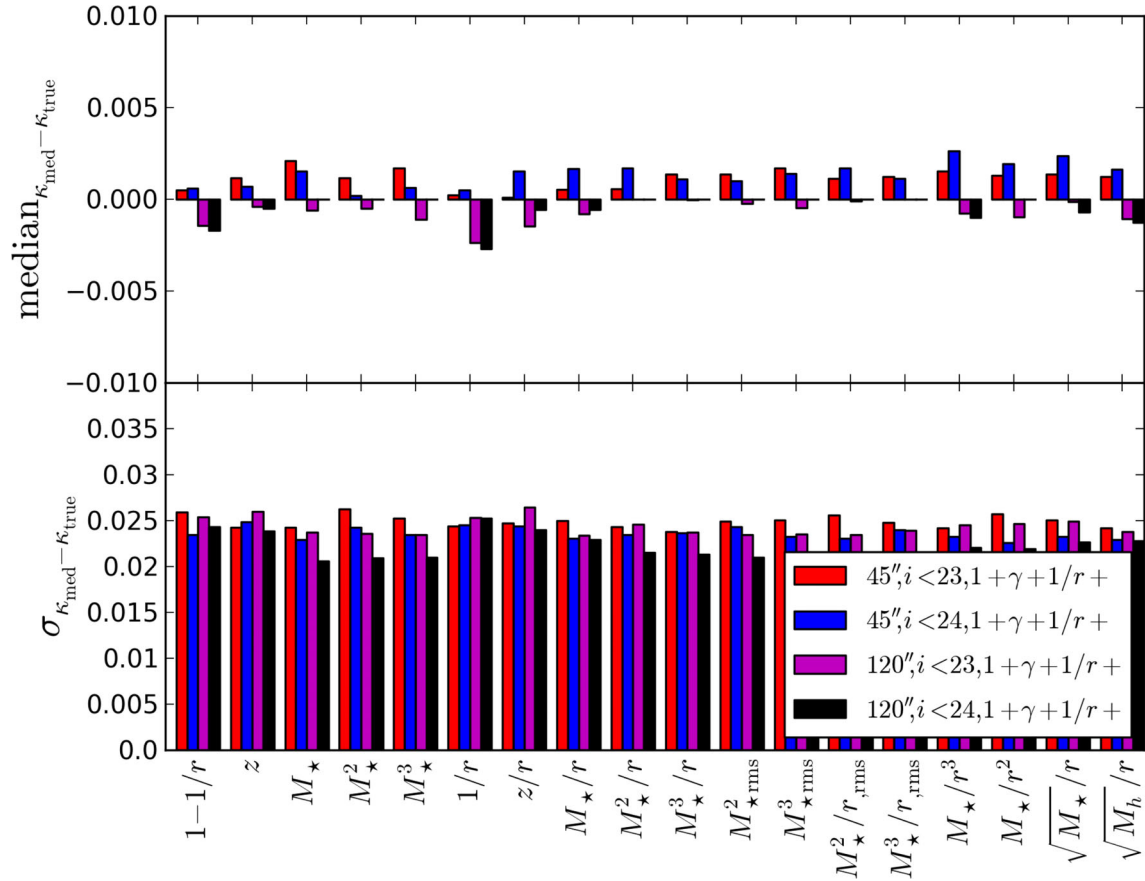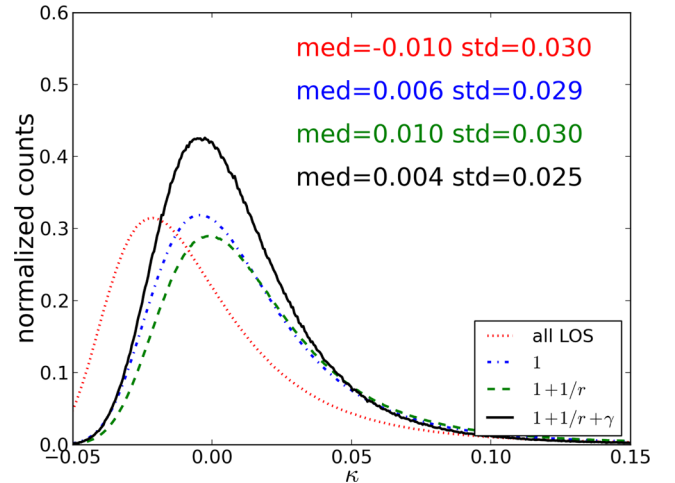
Figure 11. Medians and standard deviations of the $\kappa - \kappa_{\mathrm{med}}$ distributions for a variety of aperture radii, limiting magnitudes and conjoined weights (1, γ_{ext}, $1/r$, +). Each point in the distribution represents one of 5000 cells from the MS, which are similar in overdensity to HE 0435−1223.
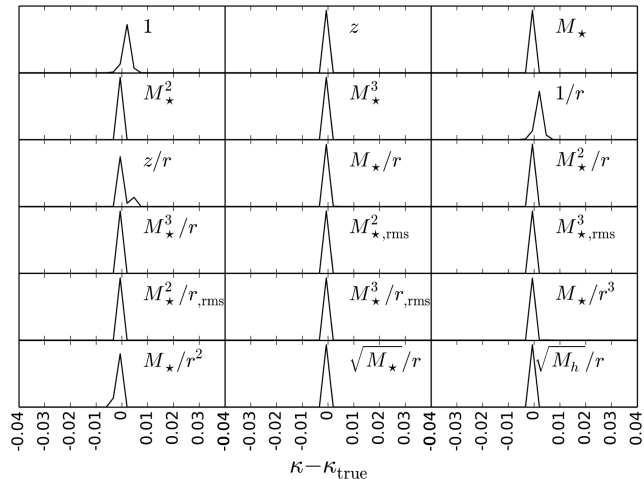
Figure 12. Products of $100\,P(\kappa - \kappa_{\mathrm{med}})$ distributions, computed in a similar way to that of HE 0435−1223 for cells of similar overdensities, using as constraints $1 + \gamma_{\mathrm{ext}} + 1/r +$ one other weight, within a 120 arcsec aperture, $i < 24$ mag. The plots for other apertures and magnitude limits are similar.

Figure 13. Example of the variation of $P(\kappa_{\mathrm{ext}})$ with the addition of constraints, for aperture radius 45 arcsec, $i < 24$ mag.

distributions by ∼0.005. This is expected, since G13 find that the use of weighted count constraints does not yield much improvement for fields of typical overdensities, such as HE 0435−1223. As a result, we do not expect further improvement if using more than four conjoined constraints. The standard deviations of each of the distributions are ∼0.025, which is similar to the values G13 find for

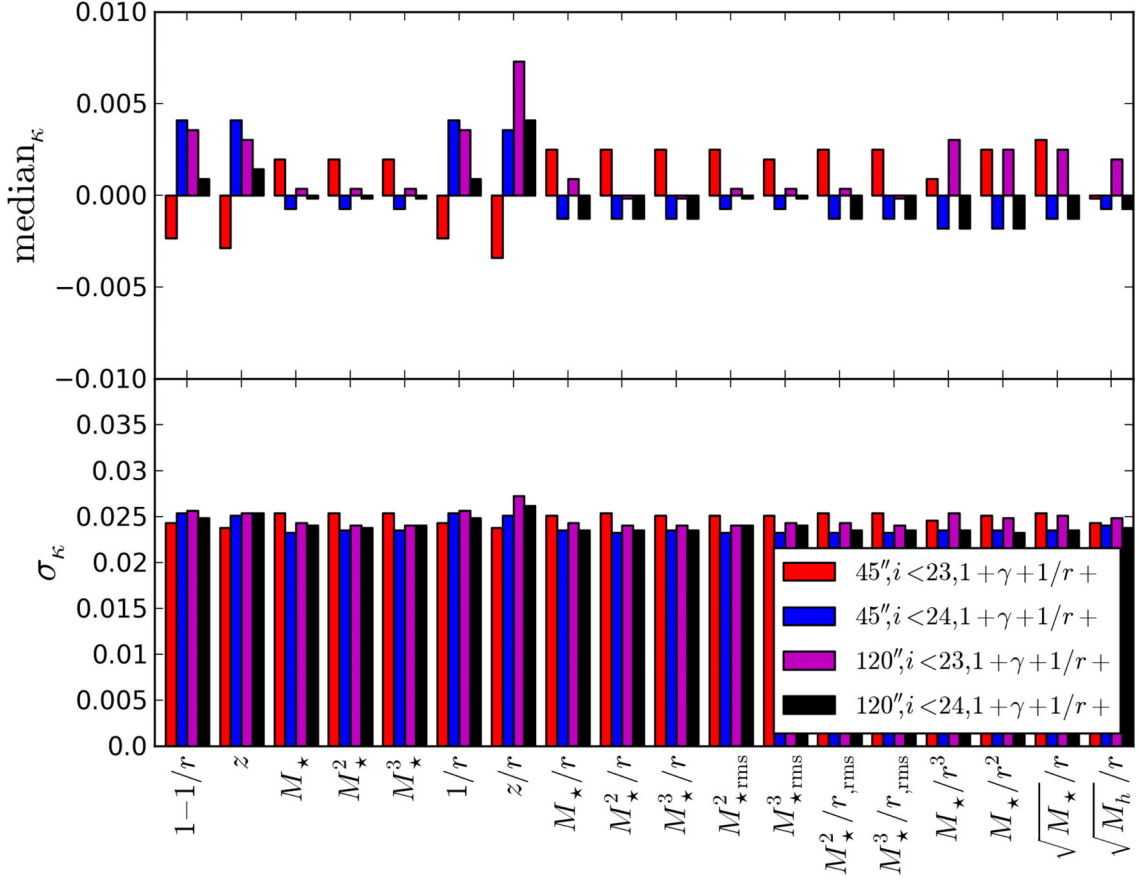fields of comparable overdensities; we note, however, that G13 did not use shear as a constraint.[10]

The shift value at which the distributions are consistent with each other, ∼0.005, even if different apertures and limiting magnitudes

---

[10] We also checked that changing the shear constraint by ∼0.025 towards lower values lowers κ_{ext} by ∼0.005.

Figure 14. Medians and standard deviations of the $P(\kappa|1, \gamma_{\mathrm{ext}}, 1/r, +)$ distributions for a variety of aperture radii, limiting magnitudes and conjoined weights, for HE 0435−1223. Here $1 - 1/r$ refers to $P(\kappa|1, \gamma_{\mathrm{ext}})$.

Table 4. $\kappa^{\mathrm{med}}_{\mathrm{ext}}$ and σ_κ for conjoined weights $1 + \gamma_{\mathrm{ext}} + 1/r + q$.

q	45 arcsec $i < 24$	45 arcsec $i < 23$	120 arcsec $i < 24$	120 arcsec $i < 23$
$1 - \frac{1}{r}$	$+0.002, 0.025$	$-0.001, 0.025$	$+0.002, 0.024$	$+0.002, 0.025$
z	$+0.003, 0.025$	$-0.004, 0.024$	$+0.001, 0.025$	$+0.002, 0.025$
$M_\star$	$-0.001, 0.023$	$+0.001, 0.025$	$-0.002, 0.023$	$-0.000, 0.024$
$M_\star^2$	$-0.002, 0.023$	$+0.002, 0.025$	$-0.002, 0.023$	$-0.000, 0.024$
$M_\star^3$	$-0.001, 0.023$	$+0.002, 0.025$	$-0.002, 0.023$	$-0.000, 0.024$
$\frac{1}{r}$	$+0.004, 0.025$	$-0.003, 0.024$	$+0.000, 0.025$	$+0.002, 0.025$
$\frac{z}{r}$	$+0.003, 0.025$	$-0.004, 0.024$	$+0.004, 0.026$	$+0.007, 0.027$
$\frac{M_\star}{r}$	$-0.002, 0.023$	$+0.002, 0.025$	$-0.002, 0.023$	$+0.000, 0.024$
$\frac{M_\star^2}{r}$	$-0.002, 0.023$	$+0.002, 0.025$	$-0.002, 0.023$	$-0.001, 0.024$
$\frac{M_\star^3}{r}$	$-0.002, 0.023$	$+0.002, 0.025$	$-0.002, 0.023$	$-0.001, 0.024$
$M_{\star,\mathrm{rms}}^2$	$-0.002, 0.023$	$+0.002, 0.025$	$-0.002, 0.023$	$-0.000, 0.024$
$M_{\star,\mathrm{rms}}^3$	$-0.002, 0.023$	$+0.001, 0.025$	$-0.002, 0.023$	$-0.001, 0.024$
$\frac{M_\star^2}{r},\mathrm{rms}$	$-0.002, 0.023$	$+0.002, 0.025$	$-0.002, 0.023$	$-0.001, 0.024$
$\frac{M_\star^3}{r},\mathrm{rms}$	$-0.002, 0.023$	$+0.002, 0.025$	$-0.002, 0.023$	$-0.001, 0.024$
$\frac{M_\star}{r^3}$	$-0.002, 0.023$	$+0.001, 0.025$	$-0.002, 0.023$	$+0.002, 0.025$
$\frac{M_\star}{r^2}$	$-0.002, 0.023$	$+0.002, 0.025$	$-0.002, 0.023$	$+0.002, 0.025$
$\frac{\sqrt{M_\star}}{r}$	$-0.002, 0.023$	$+0.002, 0.025$	$-0.002, 0.023$	$+0.002, 0.025$
$\frac{\sqrt{M_h}}{r}$	$-0.001, 0.023$	$-0.001, 0.024$	$-0.001, 0.024$	$+0.001, 0.025$

Note. The pairs on each column represent $(\kappa^{\mathrm{med}}_{\mathrm{ext}}, \sigma_\kappa)$. Here $q = 1 - 1/r$ refers to conjoined weights $1 + \gamma_{\mathrm{ext}}$.

are considered, corresponds to ∼0.5 per cent impact on H_0, according to equation (3). Combined with the result from Section 6.2, that our technique is free of biases, this means that our approach is insensitive to the exact choice of aperture and limiting magnitude, among those we explored, at this level. That is, our small, bright limit is already large and deep enough for our analysis. In contrast, as we consider larger and larger apertures, we would expect that we wash away signal, unless we weigh by something steeper than $1/r$, because we include larger numbers of galaxies which may be too distant to contribute to κ_{ext}^{true}. Given large enough apertures, they will tend to an unweighted count ratio of unity regardless of the field. The same argument would hold for deeper magnitudes, except that we implement a cut at the redshift of the source quasar, so going deeper does not imply that we contaminate the signal. The consistency of our results indicates that our large, deep limits are still sensitive to the desired κ_{ext}^{true}. Finally, the mutual consistency of the distributions for the two limiting magnitudes also ensures that our results are not affected by possible incompleteness.[11]

We note that the small κ_{ext} value we measure, well consistent with zero, is also in agreement with the weak lensing upper limit on convergence <0.04 for this system (Tihhonova et al., in preparation), and the unlikely existence of large structures such as groups, significant enough to boost the convergence (H0LiCOW Paper II).

8 CONCLUSIONS AND FUTURE WORK

In this work, we aimed to estimate a robust probability distribution function of the external convergence for HE 0435−1223, in order to enable the use of this lens system as an accurate probe of H_0. We used spectroscopy and multiband images of the HE 0435−1223 field, and we used the wide component of CFHTLenS as a control field. Building on the work by G13, we refined the method in order to cope with the large fraction of masks in our control field, and we also used more robust medians rather than sums in order to compare weighted counts. We thoroughly explored sources of error in our data sets, such as mask coverage, galaxy–star classification, detection efficiency etc.; we propagated these into the computation of weighted count ratios, finding that the HE 0435−1223 field is more overdense, in terms of number counts, than previously estimated. We used the whole extent of the MS to simulate photometric data of the same quality, and connect the MS lensing convergence catalogue to synthetic weighted count ratios estimated in a similar way. We then estimated the probability distribution function of the external convergence for fields similar in overdensity to HE 0435−1223, in a Bayesian, unbiased way.

We considered multiple aperture radii and limiting magnitudes, and tested them using the MS, finding that a 45 arcsec aperture and a limiting magnitude of $i \leq 23$ provide enough spatial coverage and depth to estimate the distribution of external convergence via the weighted counts technique. We find that our different estimates are consistent with each other at a level of ∼0.005, corresponding to ∼0.5 per cent impact on H_0. Our estimate which is least affected by photometric redshifts and stellar mass uncertainties, $P(\kappa_{ext}|\zeta_{q_{gal}}, \zeta_{q_{1/r}}, \zeta_{\gamma ext})$, has a median of 0.004, and a standard deviation of 0.025. This uncertainty contributes ∼2.5 per cent rms error to the value of H_0. We intend to employ the techniques developed

in this paper for the analysis of the other H0LiCOW lens systems. In particular, HE 0435−1223 is a rather typical line of sight, and we expect that lenses residing in comparatively overdense fields will benefit more from the use of additional constraints including photometric redshifts and stellar masses.

Throughout this work, we have made extensive use of the MS. The weighted count ratios technique is designed to minimize our reliance on a particular simulation, but it will be useful to repeat this analysis by using simulations for different cosmologies and galaxy models to test any remaining dependencies. However, we expect such dependencies to be small, given that the external convergence we measure is close to zero. Assuming a simple linear deterministic galaxy bias model, the convergence inferred from a given relative galaxy number overdensity scales roughly with the mean matter density parameter Ω_m and the matter density fluctuation amplitude σ_8 (see Appendix D). Therefore, for example, $\kappa_{ext}^{med, Planck} \propto \kappa_{ext}^{med, MS} \Omega_m^{Planck} \sigma_8^{Planck}/(\Omega_m^{MS} \sigma_8^{MS}) \sim 1.13 \kappa_{ext}^{med, MS}$. For $\kappa_{ext}^{med, MS} = 0.004$, this corresponds to $\lesssim 0.001$ impact. We leave further checks for future work, as other simulations with convergence maps become available.

Recently, McCully et al. (2017) presented a technique of reconstructing the external convergence without relying on a particular simulation, through a direct modelling of the field. This has the potential of further reducing the uncertainty on the external convergence. This work has produced the galaxy catalogues necessary for a future implementation of that technique. While we have accounted in this work for the presence of voids, groups and clusters statistically, through the use of the MS, our catalogue products are also used in separate works (H0LiCOW Paper II and Tihhonova et al., in preparation) to directly identify such structures.

---

[11] Though an estimate of completeness is not available for CFHTLenS, for the shallower CFHTLS parent catalogue this is 80 per cent for extended sources of $i \sim 23.4$ mag, according to http://www.cfht.hawaii.edu/Science/CFHLS/T0007/T0007-docsu12.html

This work is based in part on observations obtained with MegaPrime/MegaCam, a joint project of CFHT and CEA/IRFU, at the CFHT which is operated by the National Research Council (NRC) of Canada, the Institut National des Sciences de l'Univers of the Centre National de la Recherche Scientifique (CNRS) of France, and the University of Hawaii. It is also based in part on observations made with the *Spitzer* Space Telescope, which is operated by the Jet Propulsion Laboratory, California Institute of Technology under a contract with NASA, and on observations obtained at the Gemini Observatory, which is operated by the Association of Universities for Research in Astronomy, Inc., under a cooperative agreement with the NSF on behalf of the Gemini partnership: the National Science Foundation (United States), the National Research Council (Canada), CONICYT (Chile), the Australian Research Council (Australia), Ministério da Ciência, Tecnologia e Inovação (Brazil) and Ministerio de Ciencia, Tecnología e Innovación Productiva (Argentina).

The authors recognize and acknowledge the very significant cultural role and reverence that the summit of Mauna Kea has always had within the indigenous Hawaiian community. We are most fortunate to have the opportunity to conduct observations from this superb mountain.

This work made use of Astropy (Astropy Collaboration et al. 2013). TOPCAT (Taylor 2005) was used for catalogue matching. The codes developed during the course of this work are publicly available at https://github.com/eduardrusu/zMstarPDF.

REFERENCES

Astropy Collaboration et al., 2013, A&A, 558, A33
Behroozi P. S., Conroy C., Wechsler R. H., 2010, ApJ, 717, 379
Benítez N., 2000, ApJ, 536, 571
Bertin E., 2006, ASP Conf. Ser. Vol. 351, Astronomical Data Analysis Software and Systems XV. Astron. Soc. Pac., San Francisco, p. 112
Bertin E., Arnouts S., 1996, A&AS, 117, 393
Bertin E., Mellier Y., Radovich M., Missonnier G., Didelon P., Morin B., 2002, ASP Conf. Ser. Vol. 281, Astronomical Data Analysis Software and Systems XI. Astron. Soc. Pac., San Francisco, p. 228
Bonvin V. et al., 2017, MNRAS, 465, 4914
Boulade O. et al., 2003, in Iye M., Moorwood A. F. M., eds, Proc. SPIE Conf. Ser. 4841, Instrument Design and Performance for Optical/Infrared Ground-based Telescopes. SPIE, Bellingham, p. 72
Bower R. G., Benson A. J., Malbon R., Helly J. C., Frenk C. S., Baugh C. M., Cole S., Lacey C. G., 2006, MNRAS, 370, 645
Brammer G. B., van Dokkum P. G., Coppi P., 2008, ApJ, 686, 1503
Bruzual G., Charlot S., 2003, MNRAS, 344, 1000
Buton C. et al., 2012, yCat, 354, 90008
Chabrier G., 2003, PASP, 115, 763
Collett T. E., Cunnington S. D., 2016, MNRAS, 462, 3255
Collett T. E. et al., 2013, MNRAS, 432, 679
De Lucia G., Blaizot J., 2007, MNRAS, 375, 2
Erben T. et al., 2013, MNRAS, 433, 2545
Falco E. E., Gorenstein M. V., Shapiro I. I., 1985, ApJ, 289, L1
Fassnacht C. D., Gal R. R., Lubin L. M., McKean J. P., Squires G. K., Readhead A. C. S., 2006, ApJ, 642, 30
Fassnacht C. D., Koopmans L. V. E., Wong K. C., 2011, MNRAS, 410, 2167
Fazio G. G. et al., 2004, ApJS, 154, 10
Garilli B. et al., 2008, A&A, 486, 683
Greene Z. S. et al., 2013, ApJ, 768, 39 (G13)
Guo Q. et al., 2011, MNRAS, 413, 101
Gwyn S. D. J., 2012, AJ, 143, 38
Heymans C. et al., 2012, MNRAS, 427, 146
Hilbert S., Hartlap J., White S. D. M., Schneider P., 2009, A&A, 499, 31

Hildebrandt H. et al., 2010, A&A, 523, A31
Hildebrandt H. et al., 2012, MNRAS, 421, 2355
Hodapp K. W. et al., 2003, PASP, 115, 1388
Ichikawa T. et al., 2006, in McLean I. S., Iye M., eds, Proc. SPIE Conf. Ser. Vol. 6269, Ground-Based and Airborne Instrumentation for Astronomy. SPIE, Bellingham, p. 626916
Ilbert O. et al., 2006, A&A, 457, 841
Ilbert O. et al., 2010, ApJ, 709, 644
Keeton C. R., Zabludoff A. I., 2004, ApJ, 612, 660
Le Fèvre O. et al., 2005, A&A, 439, 845
Lucy L. B., 1974, AJ, 79, 745
McCully C., Keeton C. R., Wong K. C., Zabludoff A. I., 2017, ApJ, 836, 141
Merlin E. et al., 2015, A&A, 582, A15
Miyazaki S. et al., 2002, PASJ, 54, 833
Momcheva I., Williams K., Keeton C., Zabludoff A., 2006, ApJ, 641, 169
Momcheva I. G., Williams K. A., Cool R. J., Keeton C. R., Zabludoff A. I., 2015, ApJS, 219, 29
Morgan N. D., Kochanek C. S., Pevunova O., Schechter P. L., 2005, AJ, 129, 2531
Refsdal S., 1964, MNRAS, 128, 307
Richardson W. H., 1972, J. Opt. Soc. Am., 62, 55
Schlafly E. F., Finkbeiner D. P., 2011, ApJ, 737, 103
Schneider P., Sluse D., 2013, A&A, 559, A37
Scoville N. et al., 2007, ApJS, 172, 1
Sluse D., Hutsemékers D., Courbin F., Meylan G., Wambsganss J., 2012, A&A, 544, A62
Sluse D. et al., 2017, MNRAS, preprint (arXiv:1607.00382)
Springel V. et al., 2005, Nature, 435, 629
Suyu S. H., Marshall P. J., Auger M. W., Hilbert S., Blandford R. D., Koopmans L. V. E., Fassnacht C. D., Treu T., 2010, ApJ, 711, 201
Suyu S. H. et al., 2013, ApJ, 766, 70
Suyu S. H. et al., 2017, MNRAS, preprint (arXiv:1607.00017)
Suzuki R. et al., 2008, PASJ, 60, 1347
Taylor M. B., 2005, ASP Conf. Ser. Vol. 347. Astronomical Data Analysis Software and Systems XIV. Astron. Soc. Pac., San Francisco, p. 29
Treu T., Marshall P. J., 2016, A&AR, 24, 11
Velander M. et al., 2014, MNRAS, 437, 2111
Wisotzki L., Christlieb N., Bade N., Beckmann V., Köhler T., Vanelle C., Reimers D., 2000, A&A, 358, 77
Wisotzki L., Schechter P. L., Bradt H. V., Heinmüller J., Reimers D., 2002, A&A, 395, 17
Wong K. C., Keeton C. R., Williams K. A., Momcheva I. G., Zabludoff A. I., 2011, ApJ, 726, 84
Wong K. C. et al., 2017, MNRAS, 465, 4895
Yagi M., Gu L., Fujita Y., Nakazawa K., Akahori T., Hattori T., Yoshida M., Makishima K., 2013a, ApJ, 778, 91
Yagi M. S., Nao, Yamanoi H., Furusawa H., Nakata F., Komiyama Y., 2013b, PASJ, 65, 22

SUPPORTING INFORMATION

Supplementary data are available at *MNRAS* online.

Table A1.
Table A2.

Please note: Oxford University Press is not responsible for the content or functionality of any supporting materials supplied by the authors. Any queries (other than missing material) should be directed to the corresponding author for the article.

APPENDIX A: CATALOGUES OF GALAXIES AND DERIVED PROPERTIES

**Table A1.** Photometric properties of the $i \leq 23$ galaxies inside 45 arcsec of HE 0435−1223.

RA	Dec.	i_{tot}	Sep	u	g	r	i	J	H	K_s	3.6 μm	4.5 μm	5.7 μm	7.9 μm
69.57430	−12.28945	18.64	43.88	22.55 ± 0.02	20.93 ± 0.01	19.45 ± 0.01	18.73 ± 0.01	18.01 ± 0.01	17.71 ± 0.01	17.48 ± 0.01	17.90 ± 0.01	18.21 ± 0.27	18.36 ± 0.30	19.19 ± 0.35
69.55442	−12.28233	20.12	32.48	22.47 ± 0.02	21.44 ± 0.01	20.60 ± 0.01	20.16 ± 0.01	19.32 ± 0.01	18.77 ± 0.01	18.53 ± 0.01	18.93 ± 0.01	18.80 ± 0.27	18.96 ± 0.30	17.53 ± 0.35
69.55975	−12.28627	20.21	9.05	21.89 ± 0.01	21.28 ± 0.01	20.49 ± 0.01	20.23 ± 0.01	19.61 ± 0.01	19.15 ± 0.02	19.15 ± 0.01	19.56 ± 0.01	19.51 ± 0.27	19.80 ± 0.30	18.73 ± 0.35
69.56122	−12.28845	20.43	4.32	22.81 ± 0.02	22.19 ± 0.01	21.37 ± 0.01	20.50 ± 0.01	19.40 ± 0.01	18.97 ± 0.01	18.72 ± 0.01	18.65 ± 0.01	19.08 ± 0.27	19.27 ± 0.30	18.96 ± 0.35
69.55652	−12.27911	20.73	35.83	23.41 ± 0.04	22.37 ± 0.01	21.28 ± 0.01	20.81 ± 0.01	19.99 ± 0.01	19.58 ± 0.02	19.42 ± 0.01	19.86 ± 0.01	19.99 ± 0.27	20.29 ± 0.30	19.81 ± 0.35
69.56013	−12.28546	21.03	9.85	23.77 ± 0.04	22.76 ± 0.01	21.59 ± 0.01	21.05 ± 0.01	20.18 ± 0.01	19.71 ± 0.02	19.60 ± 0.01	19.88 ± 0.01	20.09 ± 0.27	20.32 ± 0.30	19.48 ± 0.35
69.55710	−12.29236	21.04	24.50	22.66 ± 0.02	22.20 ± 0.01	21.60 ± 0.01	21.11 ± 0.01	20.75 ± 0.01	20.36 ± 0.04	20.22 ± 0.01	20.37 ± 0.01	20.74 ± 0.27	20.68 ± 0.31	20.69 ± 0.37
69.55370	−12.28414	21.19	31.57	23.61 ± 0.04	22.81 ± 0.01	21.59 ± 0.01	21.18 ± 0.01	20.37 ± 0.01	19.96 ± 0.02	19.86 ± 0.01	20.28 ± 0.01	20.35 ± 0.27	20.50 ± 0.30	19.78 ± 0.35
69.57109	−12.27948	21.24	43.15	23.34 ± 0.03	22.50 ± 0.01	21.61 ± 0.01	21.29 ± 0.01	20.74 ± 0.01	20.44 ± 0.03	20.20 ± 0.01	20.79 ± 0.01	20.84 ± 0.27	20.62 ± 0.30	20.45 ± 0.36
69.55553	−12.29793	21.67	43.84	23.27 ± 0.03	22.83 ± 0.01	22.06 ± 0.01	21.81 ± 0.01	21.54 ± 0.02	22.99 ± 0.40	21.58 ± 0.03	21.71 ± 0.03	22.14 ± 0.28	22.41 ± 0.44	–
69.56258	−12.28962	21.73	7.87	26.51 ± 0.41	24.66 ± 0.04	22.92 ± 0.01	21.68 ± 0.01	20.52 ± 0.01	20.11 ± 0.02	19.77 ± 0.01	19.61 ± 0.03	20.03 ± 0.27	20.44 ± 0.30	20.38 ± 0.36
69.56038	−12.28351	22.00	15.47	27.31 ± 0.75	24.70 ± 0.04	23.10 ± 0.01	22.02 ± 0.01	20.84 ± 0.01	20.34 ± 0.03	20.17 ± 0.01	19.99 ± 0.01	20.44 ± 0.27	20.38 ± 0.30	20.66 ± 0.37
69.56071	−12.28990	22.16	9.71	27.20 ± 0.81	24.68 ± 0.05	23.01 ± 0.01	22.07 ± 0.01	20.77 ± 0.01	20.45 ± 0.04	20.05 ± 0.01	19.84 ± 0.01	20.27 ± 0.27	20.35 ± 0.30	20.76 ± 0.38
69.57321	−12.29053	22.31	40.96	24.04 ± 0.06	23.68 ± 0.02	22.69 ± 0.01	22.23 ± 0.02	22.12 ± 0.03	21.45 ± 0.09	21.61 ± 0.03	21.88 ± 0.03	22.22 ± 0.28	–	–
69.55510	−12.27773	22.73	42.73	26.06 ± 0.20	24.70 ± 0.03	23.48 ± 0.01	22.90 ± 0.02	22.08 ± 0.02	22.08 ± 0.11	21.56 ± 0.02	21.75 ± 0.02	22.00 ± 0.27	21.94 ± 0.35	–
69.55990	−12.28712	22.81	7.47	24.26 ± 0.04	23.81 ± 0.02	23.42 ± 0.01	22.91 ± 0.02	22.42 ± 0.02	22.26 ± 0.14	22.32 ± 0.03	21.70 ± 0.03	21.92 ± 0.27	22.81 ± 0.53	20.33 ± 0.36
69.55017	−12.29207	22.89	44.68	26.61 ± 0.35	26.10 ± 0.12	24.12 ± 0.01	22.99 ± 0.02	21.74 ± 0.01	20.81 ± 0.03	20.84 ± 0.01	20.56 ± 0.01	21.05 ± 0.27	20.94 ± 0.31	–
69.56423	−12.28099	22.93	24.77	24.46 ± 0.05	23.82 ± 0.03	23.29 ± 0.01	23.07 ± 0.02	22.55 ± 0.03	22.40 ± 0.15	22.41 ± 0.04	23.12 ± 0.25	23.58 ± 0.36	22.08 ± 0.41	22.05 ± 0.63
69.55569	−12.28037	22.96	33.95	24.27 ± 0.04	23.81 ± 0.02	23.74 ± 0.01	23.34 ± 0.03	22.65 ± 0.03	21.70 ± 0.09	22.34 ± 0.04	21.21 ± 0.03	21.06 ± 0.27	21.15 ± 0.32	21.35 ± 0.42
69.56407	−12.29717	22.98	35.52	23.69 ± 0.03	23.53 ± 0.01	23.34 ± 0.01	22.98 ± 0.01	22.40 ± 0.02	21.94 ± 0.10	21.91 ± 0.02	21.58 ± 0.02	21.90 ± 0.27	22.43 ± 0.42	20.76 ± 0.38

Note. The complete catalogue of $i \leq 24$ galaxies inside 120 arcsec is available as online material, and the *ugri* photometry for the complete Subaru/Suprime-Cam FOV is available upon request. Galaxies covered by the masks in Fig. 1, except for the nearest companion inside 5 arcsec of HE 0435−1223, are not reported. Here i_{tot} is the SEXTRACTOR *mag_auto* with detections in *i* band, and the rest are *mag_iso* magnitudes with detections in the *r* band, corrected by adding *mag_auto_r* − *mag_iso_r*. Reported magnitudes are corrected for atmospheric (when necessary) and galactic extinction, but not for the zero-point offsets estimated by BPZ (with the exception of i_{tot}; see text). These offsets are: $\Delta u = -0.07$, $\Delta g = 0.12$, $\Delta r = 0.05$, $\Delta i = -0.02$, $\Delta J = -0.01$, $\Delta H = 0.06$ and $\Delta K_s = 0.09$. For the IRAC channels, errors include those from the EAZY template error function.

Table A2. Inferred redshifts, stellar and halo masses of the $i \leq 23$ galaxies inside 45 arcsec of HE 0435−1223.

RA	Dec.	Sep	ZSPEC/BPZ	z_{16} per cent	z_{84} per cent	$\log M_\star$	$\log M_{halo}$	RA	Dec.	Sep	ZSPEC/BPZ	z_{inf}	z_{sup}	$\log M_\star$	$\log M_{halo}$
69.57430	−12.28945	43.88	0.515	–	–	11.1500	14.0037	69.56258	−12.28962	7.87	0.781	–	–	10.5502	12.8158
69.55442	−12.28233	32.48	0.277	–	–	9.9580	12.1143	69.56038	−12.28351	15.47	0.702	–	–	10.4472	12.6788
69.55975	−12.28627	9.05	0.419	–	–	9.9445	12.1451	69.56071	−12.28990	9.71	0.779	–	–	10.7420	13.0907
69.56122	−12.28845	4.32	0.782	–	–	10.9000	13.3647	69.57321	−12.29053	40.96	0.48	0.41	0.55	9.2501	11.7876
69.55652	−12.27911	35.83	0.41	0.34	0.48	10.1380	12.2910	69.55510	−12.27773	42.73	0.36	0.29	0.43	9.3728	11.8225
69.56013	−12.28546	9.85	0.457	–	–	10.3990	12.5692	69.55990	−12.28712	7.47	0.64	0.56	0.72	9.3000	11.8362
69.55710	−12.29236	24.50	0.678	–	–	9.8689	12.1570	69.55017	−12.29207	44.68	0.81	0.72	0.90	10.3029	12.5396
69.55370	−12.28414	31.57	0.419	–	–	10.2032	12.3521	69.56423	−12.28099	24.77	0.25	0.19	0.31	8.5401	11.4583
69.57109	−12.27948	43.15	0.37	0.30	0.44	9.5001	11.8830	69.55569	−12.28037	33.95	0.87	0.78	0.96	9.1534	11.8060
69.55553	−12.29793	43.84	0.488	–	–	9.3000	11.8110	69.56407	−12.29717	35.52	1.01	0.91	1.11	9.6334	12.1157

Note. The complete catalogue of $i \leq 24$ galaxies inside 120 arcsec is available as online material, and that of the complete Subaru/Suprime-Cam FOV, based on *ugri* photometry, is available upon request. Where z_{16} per cent and z_{84} per cent values are not given, spectroscopic redshifts are available. Photometric redshift values correspond to the peak of the probability distributions, and logarithmic mass values correspond to the medians of the probability distributions estimated with LE PHARE. The typical uncertainty given by LE PHARE (including IRAC photometry) for $M_\star$ is ∼0.05 dex.
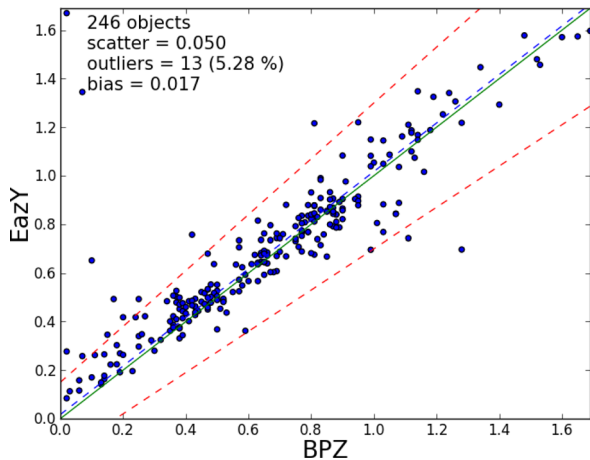
Figure B1. Comparison of photometric redshift estimated with BPZ and EAZY from *ugriJHK$_s$* photometry, for the $i \leq 24$ galaxies within 120 arcsec, without available spectroscopic redshifts.

APPENDIX B: EXPLORING SYSTEMATICS AND SOURCES OF NOISE IN THE ESTIMATION OF WEIGHTED COUNT RATIOS

When measuring the weighted count ratios as described in Section 5.1, we account for several factors and estimate how much they contribute to the total uncertainty:

(i) Sample variance. To test the extent to which we are affected by sample variance, as well as by different fractions of stars in the CFHTLenS fields, we do not combine the W1–W4 fields, but measure overdensities for each of them separately. W4 is known to contain a larger fraction of stars (Hildebrandt et al. 2012), and this may impact our results, given our galaxy–star classification, which assumes that all faint objects are galaxies (Section 3). We also expect this to be the case for W2, given its low galactic latitude.[12]

(ii) Fraction of masks. Using CFHTLenS cells with a substantial fraction of their areas covered by masks may introduce large Poisson noise. To estimate this effect, we exclude all cells that have more than 25 and 50 per cent, respectively, of their areas masked. This results in eliminating 40 per cent, 32 per cent of the cells (45 arcsec apertures), and 36 per cent, 24 per cent of the cells (120 arcsec apertures), respectively.

(iii) Limiting magnitude and aperture radius. To quantify the dependence of our results on the aperture radius and limiting magnitude, we also consider limits of 45-arcsec radius (used by G13) and $i \leq 23$ mag (S/N $\sim$30), in addition to 120 arcsec and $i \leq 24$.

(iv) Detection efficiency. In order to avoid biases when estimating weighted counts relative to CFHTLenS, and in view of the similarity

between our *i*-band data for HE 0435−1223 and the CFHTLenS *i* band, we used the same detection parameters employed for the latter. However, galaxy counts at the limiting magnitude are sensitive to the detection parameters, and we found that by changing the DETECT_THRESHOLD parameter in SEXTRACTOR from 1.5 to 2.5, we obtain more robust detections. We therefore consider the scatter between the two detection runs, where for each one we compute weighted ratios for all weights.

(v) Detections at the limiting magnitude. Due to uncertainties in the photometry at the limiting magnitude, some galaxies above the magnitude cut are in fact wrongly included in the cut, and vice versa. This may bias the results. Therefore for all galaxies in the HE 0435−1223 field we consider a Gaussian around their SEXTRACTOR-measured *i*-band magnitude, with a standard deviation equal to the size of the photometric error bar, and randomly sample from this to test if the galaxy survives the colour cut. We do this for each *i* cell in a CHFTLenS WX field, as we compute $\zeta_q^{WX} \equiv \{W_q^{lens,mask_i}/W_q^{i \in WX}\}$. It is unnecessary to do the same for the galaxies inside CFHTLenS, due to the large number of cells.

(vi) Cell number dependence on the aperture radius. When considering a larger aperture radius around the lens system, and therefore a larger cell size, there are comparatively fewer contiguous non-overlapping cells spanning CFHTLenS. As a result, the ζ_q distribution will look noisy. To avoid this, we allow cells to partially overlap, with larger overlapping fraction for larger apertures. In practice, we use two equally spaced overlaps along each dimension of the 45-arcsec-length cells (i.e. along each dimension in the grid, we consider cells centred at length/2, 2 × length/2, 3 × length/2 etc.), and five overlaps for the 120-arcsec-length cells, respectively.

(vii) Different photometric redshift codes, and the importance of the IRAC bands. We include the scatter in the overdensities measured when using BPZ and EAZY separately, to compute photometric redshifts. This potentially affects more than just the weights explicitly incorporating redshift, since we do a cut at the source redshift, and the redshift values also affect the goodness-of-fit used to separate stars from galaxies. We also compute weights for stellar masses calculated with the inclusion of the IRAC channels, as well as without.

(viii) Accounting for the $P(z)$ and $P(M_\star|z)$ of an individual galaxy. Instead of just using the best-fitting photometric redshift and median stellar mass for each galaxy in the HE 0435−1223 field, we sample 10 times from the galaxy's redshift probability distribution, and compute the associated stellar mass (for which we also sample from the distribution returned by LE PHARE). We then compute ζ_q^{WX} for each of these. Again, it is not necessary to do this for the galaxies inside CFHTLenS, due to the large number of cells, which are only used once.

---

[12] We used the plots available at http://www.iac.es/proyecto/frida/skyCoverage.html to estimate the relative number of stars, given the galactic coordinates of each field.
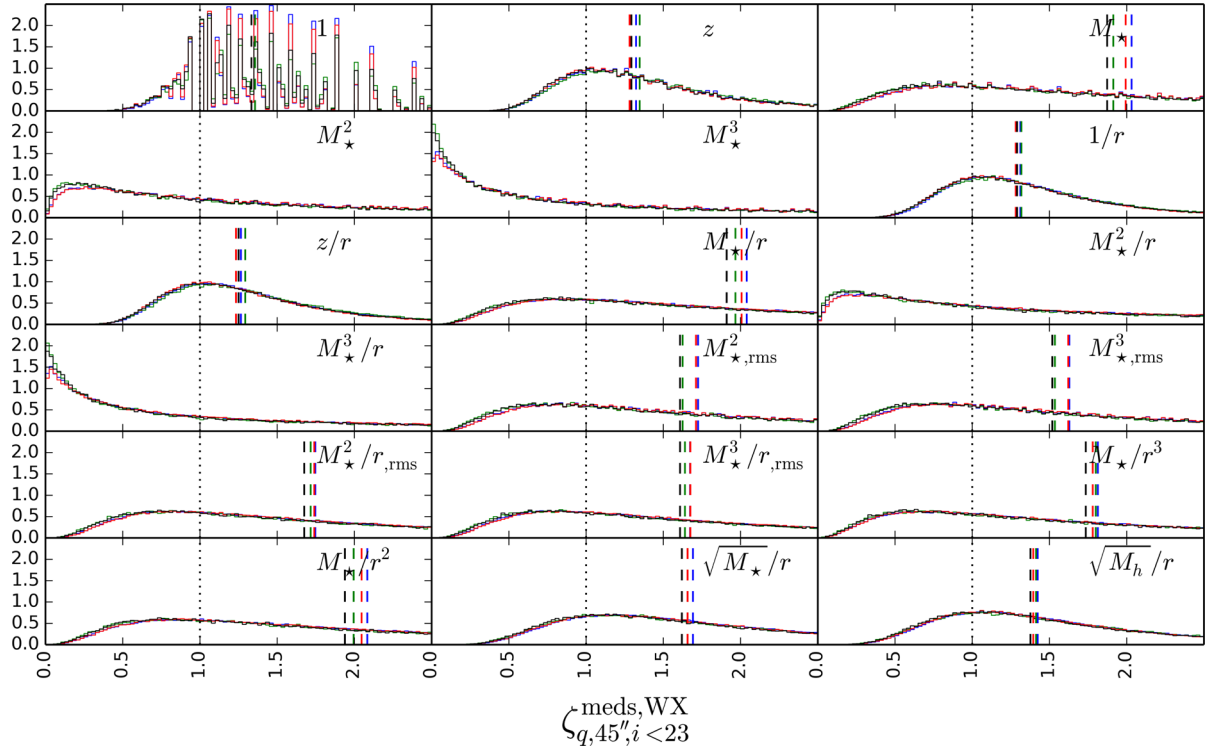
Figure B2. Histograms of weighted count ratios for all $\zeta_q^{\mathrm{meds,WX}}$ weights, for galaxies inside a 45-arcsec-radius aperture and $i \leq 23$. We use the plotting range and colours from Fig. 5. The $q = 1$ distribution appears discrete because of the small range of (positive integer) galaxy counts inside this small aperture and bright magnitude limit.
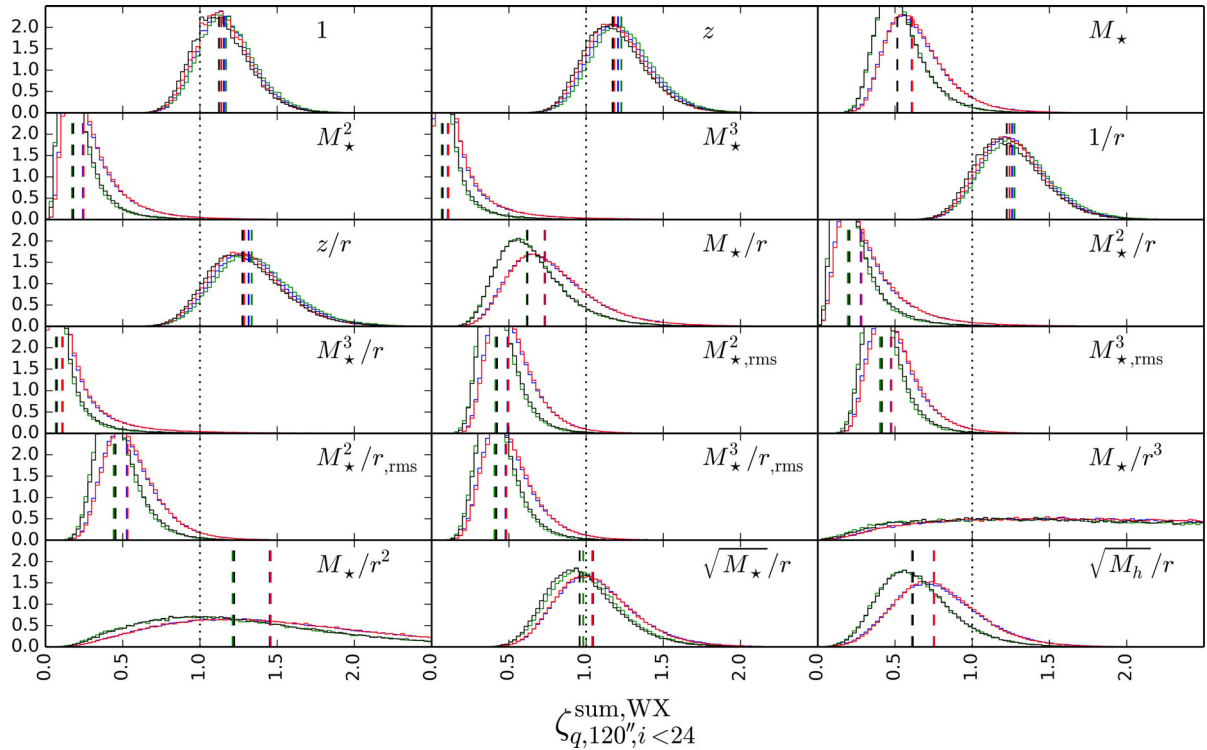
Figure B3. Histograms of weighted count ratios for all $\zeta_q^{\mathrm{sum,WX}}$ weights, for galaxies inside a 120-arcsec-radius aperture and $i \leq 24$. We use the plotting range and colours from Fig. 5.

APPENDIX C: DETAILS ON INFERRING WEIGHTED COUNT RATIOS FROM THE MS

Even though we have made every effort to analyse the simulated data in the same manner as the real data, this was not always possible, due to inherent differences and computational reasons. Here we present details of our weighted count ratios estimation from the MS, and the way the approach differs from the real data.

(i) The MS catalogues represent a pure and complete sample of galaxies, whereas this is not the case in the real data. As a result, we randomly inject stars and remove galaxies, mirroring the contamination and incompleteness found in the real data. For this, we use the contamination and incompleteness fractions estimated in fig. 9 of Hildebrandt et al. (2012) for the CFHTLenS W1 field, as a function of magnitude. We considered 500 real stars for each 0.5 mag bin from CFHTLenS, and computed for these stars 'redshifts' with BPZ, as well as 'stellar masses' with LE PHARE. We then selected from these based on the contamination fraction, and inserted them at random positions into each aperture of the simulation.

(ii) It is important to use all the complete spatial extent of the MS (i.e. all MS fields), as our use of multiple conjoined weights when selecting lines of sight of similar overdensities (which we describe in Section 6) implies that we are limited by the number of available κ_{ext} points found in the simulation. Each of the 64 MS fields has a corresponding 4096 × 4096 grid of convergence values (we refer to these as κ_{ext} points), with ~3.5 arcsec spacing. In Section B we described how we use overlapping cells across the CFHTLenS fields. Here we use even higher fractions of overlaps, as we centre one cell on each of the κ_{ext} points. The only exceptions are at the edges of the fields, where the apertures would fall outside the field.

(iii) Given the ~10^9 κ_{ext} points in the simulation, it is computationally expensive to estimate the weighted count ratios of each of the 45 arcsec or 120 arcsec aperture cells relative to every other cell, and take the median. In addition, the MS fields do not contain masks, in contrast to the HE 0435−1223 and CFHTLenS fields. However, as we have seen in Section 5.2, where we compared results after eliminating fields with different fractions of masks, the effect is negligible. The only masks we employ are the 5 arcsec radius inner masks around the centre of each cell (to account for the fact that in the real data we masked the HE 0435−1223 system itself, and its most nearby perturber), and the outer 45 arcsec or 120 arcsec radius representing the circular apertures. As a result, we can make an approximation in computing weighted count ratios. We compute the overdensity for each cell i simply as $\zeta_q^{i,\mathrm{MS}} \equiv W_q^i / \overline{W_q^{i \in \mathrm{MS}}}$, where $\overline{W_q^{i \in \mathrm{MS}}} = \mathrm{median}(W_q^{i \in \mathrm{MS}})$. We have checked that this redefinition is numerically indistinguishable from the one in Section 5.1, given the range spanned by W_q. We note, however, that the same approximation would not hold if we used the mean instead of the median.

(iv) Due to the JK_s FOV being slightly smaller than the 120 arcsec aperture, ~15 per cent of the galaxies around the edge of the HE 0435−1223 field do not have coverage in these bands. We neglect this in the simulations.

(v) The MS catalogues do not contain synthetic magnitudes in the IRAC bands. However, as discussed in Section 5.2, the effect that the exclusion of these bands has for the computation of weighting count ratios incorporating stellar masses is negligible.

(vi) Since we have a large number of cells, it is unnecessary to repeatedly sample from the magnitudes of the galaxies at the faint limit, like we did for the HE 0435−1223 field. We also do not sample

from the $P(z)$ and $P(M_\star)$ of each galaxy in the HE 0435−1223 like fields. Finally, we limit ourselves to the use of BPZ for estimating photometric redshifts.

(vii) The mass resolution limit of the MS means that towards the low-mass end, the distribution of galaxy masses is different in the MS, with respect to the Universe (represented here by the CFHTLenS and HE 0435−1223 fields). For example, we find that in CFHTLenS, ~35 per cent of galaxies have stellar masses $<10^9 \mathrm{M}_\odot$, and ~18 per cent have stellar masses $<10^8 \mathrm{M}_\odot$. In the MS, these fractions are 12 and 2 per cent, respectively. However, our approach of using ratios of weighted counts as opposed to absolute weighted counts is designed to minimize the impact of this difference on our results. That is, we compute ratios of weighted counts for the HE 0435−1223 field galaxies with respect to the CFHTLenS galaxies, and similarly for the MS, where we have simulated HE 0435−1223 field-like galaxies and CFHTLenS-like galaxies (i.e. in terms of the number of filters used to compute the stellar masses). Therefore, both in the case of the real galaxies and the MS galaxies, the distributions of galaxy masses in the numerator with respect to the denominator correspond to the same 'universe'.

APPENDIX D: COSMOLOGY DEPENDENCE OF THE EXTERNAL CONVERGENCE ESTIMATES

Using a simple galaxy bias model, we can obtain a rough estimate of the cosmology dependence of the external convergence inferred from weighted galaxy counts. To first order in matter density fluctuations, the convergence $\kappa(\boldsymbol{\theta}, z_\mathrm{s})$ for sources with angular image position $\boldsymbol{\theta}$ and redshift z_s can be expressed by a weighted projection of the matter density contrast δ_m along the line of sight:

$$
\begin{aligned}
\kappa(\boldsymbol{\theta}, z_\mathrm{s}) &= \frac{3 H_0^2 \Omega_\mathrm{m}}{2 c^2} \int_0^{\chi_\mathrm{s}} \mathrm{d}\chi_\mathrm{d}\, (1 + z_\mathrm{d}) \frac{f_\mathrm{ds} f_\mathrm{d}}{f_\mathrm{s}} \\
&\quad \times \delta_\mathrm{m}\left(f_\mathrm{d} \boldsymbol{\theta}, \chi_\mathrm{d}, z_\mathrm{d}\right) \\
&= \frac{3 \Omega_\mathrm{m}}{2} \int_0^{z_\mathrm{s}} \mathrm{d}z_\mathrm{d}\, (1 + z_\mathrm{d}) \frac{H_0}{H(z_\mathrm{d})} \frac{f_\mathrm{ds} f_\mathrm{d}}{f_\mathrm{s} \chi_{H_0}} \\
&\quad \times \delta_\mathrm{m}\left(f_\mathrm{d} \boldsymbol{\theta}, \chi_\mathrm{d}, z_\mathrm{d}\right).
\end{aligned}
\tag{D1}
$$

Here, c denotes the speed of light, $\chi_\mathrm{d} = \chi(z_\mathrm{d})$, $\chi_\mathrm{s} = \chi(z_\mathrm{s})$, $f_\mathrm{d} = f_K(\chi_\mathrm{d})$, $f_\mathrm{s} = f_K(\chi_\mathrm{s})$ and $f_\mathrm{ds} = f_K(\chi_\mathrm{s} - \chi_\mathrm{d})$, where $\chi(z)$ denotes the comoving line-of-sight distance for sources at redshift z, and $f_K(\chi)$ the comoving angular diameter distance for comoving line-of-sight distance χ. Furthermore, $\delta_\mathrm{m}(\boldsymbol{x}, \chi, z)$ denotes the matter density contrast at comoving transverse position $\boldsymbol{x}$, comoving line-of-sight distance χ, and cosmic epoch expressed by the redshift z. Moreover, $\chi_{H_0} = c/H_0$ denotes the Hubble distance, and $H(z)$ denotes the Hubble parameter at redshift z.

In a simple linear deterministic galaxy model, the galaxy density contrast δ_g is related to the matter density contrast δ_m by the relation:

$$
\delta_\mathrm{g}\left(f_\mathrm{d} \boldsymbol{\theta}, \chi_\mathrm{d}, z_\mathrm{d}\right) = b_\mathrm{g} \delta_\mathrm{m}\left(f_\mathrm{d} \boldsymbol{\theta}, \chi_\mathrm{d}, z_\mathrm{d}\right)
\tag{D2}
$$

with the galaxy bias parameter b_g as proportionality factor (assumed independent of redshift for simplicity). Assume that the large-scale galaxy correlations and/or power spectra have been observed and their amplitude has been quantified, e.g. by a galaxy fluctuation amplitude parameter σ_g defined as the standard deviation of the galaxy density contrast δ_m averaged over spheres of 8 Mpc. The analogous quantity for the matter density contrast is the cosmic matter fluctuation amplitude σ_8. For a given cosmological model and observed galaxy clustering amplitude, the bias parameter can

thus be expressed as $b_g = \sigma_g/\sigma_8$. Hence,

$$\kappa(\boldsymbol{\theta}, z_s) = \frac{3\Omega_m \sigma_8}{2\sigma_g} \int_0^{z_s} dz_d \, (1 + z_d) \, \frac{H_0}{H(z_d)} \frac{f_{ds} f_d}{f_s \chi_{H_0}}$$
$$\times \, \delta_g \left(f_d \boldsymbol{\theta}, \chi_d, z_d \right). \tag{D3}$$

For all considered cosmologies, f_s, f_d and f_{ds} are proportional to H_0^{-1}, and weakly varying with the cosmic mean density parameters Ω_m, Ω_Λ, etc. and equation-of-state parameters w, w_0, or w_a. Furthermore, $H(z) \propto H_0$ and weakly varying with Ω_m, Ω_Λ, w, etc. Thus, to lowest order in cosmological parameters, the convergence inferred from an observed galaxy density contrast δ_g (or similar relative galaxy density quantities such as the weighted counts ζ_q considered in this paper) can be expressed by

$$\kappa(\boldsymbol{\theta}, z_s) = \frac{\Omega_m}{\Omega_m^{(0)}} \frac{\sigma_8}{\sigma_8^{(0)}} \kappa^{(0)}(\boldsymbol{\theta}, z_s), \tag{D4}$$

where $\kappa^{(0)}(\boldsymbol{\theta}, z_s)$ denotes the inferred convergence assuming cosmological parameters $\Omega_m^{(0)}$ and $\sigma_8^{(0)}$ instead of parameters Ω_m and σ_8, respectively. Therefore, for an arbitrary function F which depends on the external convergence κ_{ext}, this implies

$$\int d\kappa_{ext} F(\kappa_{ext}, \ldots) = \int d\kappa_{ext}^{(0)} F\left(\frac{\Omega_m}{\Omega_m^{(0)}} \frac{\sigma_8}{\sigma_8^{(0)}} \kappa_{ext}^{(0)}, \ldots \right), \tag{D5}$$

where $\kappa_{ext}^{(0)}$ denotes the external convergence inferred assuming $\Omega_m^{(0)}$ and $\sigma_8^{(0)}$.

This paper has been typeset from a TeX/LaTeX file prepared by the author.